OCEANOGRAPHY

Adsorptive exchange of coccolith biominerals facilitates viral infection

Christopher T. Johns[1], Karen Grace Bondoc-Naumovitz[1†], Alexandra Matthews[1], Paul G. Matson[2‡], M. Debora Iglesias-Rodriguez[2], Alison R. Taylor[3], Heidi L. Fuchs[1], Kay D. Bidle[1]*

Marine coccolithophores are globally distributed, unicellular phytoplankton that produce nanopatterned, calcite biominerals (coccoliths). These biominerals are synthesized internally, deposited into an extracellular coccosphere, and routinely released into the external medium, where they profoundly affect the global carbon cycle. The cellular costs and benefits of calcification remain unresolved. Here, we show observational and experimental evidence, supported by biophysical modeling, that free coccoliths are highly adsorptive biominerals that readily interact with cells to form chimeric coccospheres and with viruses to form "viroliths," which facilitate infection. Adsorption to cells is mediated by organic matter associated with the coccolith base plate and varies with biomineral morphology. Biomineral hitchhiking increases host-virus encounters by nearly an order of magnitude and can be the dominant mode of infection under stormy conditions, fundamentally altering how we view biomineral-cell-virus interactions in the environment.

INTRODUCTION

Coccolith biominerals account for up to half of the ~1.6 Pg year^{-1} of calcium carbonate production in the pelagic ocean and collectively ballast and facilitate ~83% of the particulate organic carbon flux from the surface to the deep ocean. They are produced intracellularly in a Golgi-derived coccolith deposition vesicle (CDV), within which an organic baseplate scaffolds the nucleation of calcium carbonate onto a protococcolith ring (*1*). During coccolith maturation, an array of organic matter constituents (proteins, lipids, and polysaccharides) facilitates $CaCO_3$ precipitation, patterning, transport, and adherence to the cell (*2*–*5*). Fully mature coccoliths are extruded through the cell membrane and layered on the cell surface, where they interlock to form a coccosphere (*6*). The unique nanopatterning, biomineral architecture, and morphology serve to visually discriminate different coccolithophore species in both the modern ocean and sedimentary record (*7*). Coccolith morphology can even discriminate within a species, such as *Emiliania huxleyi*, the most abundant and cosmopolitan coccolithophore, for which distinct morphotypes contribute to ecosystem processes in natural populations (*8*, *9*).

Calcification is a fundamentally dynamic process, where *E. huxleyi* cells continually produce and shed coccoliths (*10*). Coccolith production rates are estimated to be ~0.8 coccoliths hour^{-1} (*11*), with each cell encased in a coccosphere containing 12 to 15 coccoliths, varying across strains and growth states (*11*, *12*). Once they are discarded, "free" coccoliths outnumber cells by orders of magnitude, ranging from 10 to 235 coccoliths percell in both laboratory cultures and the natural environment (*12*–*15*). The free coccolith: cell ratio increases markedly in response to viral infection (*5*), exposure to high light (*16*), and nutrient stress (reduced concentrations of N and P) (*17*). Coccoliths have associated organics (including a base plate) (*1*), an adsorptive nature (*5*), high density (2.7 g cm^{-3}) (*18*), and associated sinking speeds and are incorporated into particle aggregates (marine snow, transparent exopolymeric particles, and fecal pellets) (*19*, *20*). These attributes enable free coccoliths to participate in previously overlooked interactions with ecological and biogeochemical implications.

In environmental samples, *E. huxleyi* cells and other marine protists (i.e., tintinnids and foraminifera) have been observed via scanning electron microscopy (SEM) to adsorb free coccoliths from other morphotypes and/or other coccolithophore species ("xenospheres") (*18*, *21*–*23*). These observations suggest that passive, planktonic coccolith biominerals can be exchanged in the environment. While some researchers argued that they resulted from accidental incorporation of free coccoliths onto coccospheres, agglutination via tintinnids and foraminifera, and/or incorporation into fecal pellets (*22*), our laboratory experiments show that xenospheres occur naturally through a biologically mediated process and are not random artifacts generated during SEM preparation (see Results and Discussion section below). Together with previous observations that coccoliths are also highly adsorptive to viruses (*5*, *24*), it argues that free coccolith biominerals may provide an unexplored mechanism to transmit infectious viruses to *E. huxleyi* cells. Mesoscale blooms of *E. huxleyi* are routinely terminated by double-stranded DNA *Coccolithoviruses* [Emiliana huxleyi viruses (EhVs)] (*20*, *25*–*27*), but the mechanisms driving infection in oceanic environments, which present physical barriers to host-virus encounters and limit viral infectivity (*28*), are not well understood. Given that free coccoliths greatly outnumber cells (*12*–*15*), experience massive shedding events (*5*), and can facilitate enhanced encounters through differential sinking (see Results and Discussion section below), it stands to reason that they may play an unappreciated role in host-virus interactions. Here, we demonstrate that the adsorptive properties of coccoliths facilitate infection by effectively delivering infectious viruses to cells and increasing host-virus encounters over that of free viruses alone.

[1]Department of Marine and Coastal Sciences, Rutgers University, New Brunswick, NJ 08901, USA. [2]Ecology, Evolution, and Marine Biology, University of California, Santa Barbara, Santa Barbara, CA 93117, USA. [3]Department of Biology and Marine Biology, University of North Carolina Wilmington, Wilmington, NC 28403, USA.
*Corresponding author. Email: bidle@marine.rutgers.edu
†Present address: Living Systems Institute, University of Exeter, Exeter EX4 4QD, UK.
‡Present address: Environmental Sciences Division, Oak Ridge National Laboratory, Oak Ridge, TN 37831, USA.

RESULTS AND DISCUSSION

Xenospheres result from coccolith adsorption

We first compiled and quantified the incidence of xenospheres in diverse oceanic regimes from previous reports and existing datasets to establish their widespread presence and frequency (Fig. 1). An extensive survey of the scientific literature and globally distributed SEM datasets from the Mediterranean Sea, Southern Indian Ocean, Bay of Biscay, North Atlantic, and Santa Barbara Channel, some spanning ~40 years (*18*, *23*, *29*), revealed that xenospheres are common and widespread, with *E. huxleyi* cells having incorporated coccoliths from more than one morphotype of the same species and even coccoliths from different species (Fig. 1). We found examples with mixtures of type A, type O, and type overcalcified A (type OA) morphotypes (blue and purple highlighted coccoliths in Fig. 1, A, B, H, and I, which originate from different morphotypes) (*18*, *23*). We also found examples of multispecies xenospheres, whereby *E. huxleyi* incorporated coccoliths from *Syracosphaera corolla*, *Rhabdosphaera clavigera*, *Gephyrocapsa* spp., and *Discosphaera tubifera* (orange highlighted coccoliths originate from different coccolithophore species; Fig. 1, B to G and J) (*21*, *30*, *31*). Given that *E. huxleyi* cells only produce coccoliths of one morphotype (*32*), these observations suggest that xenospheres are generated via coccolith

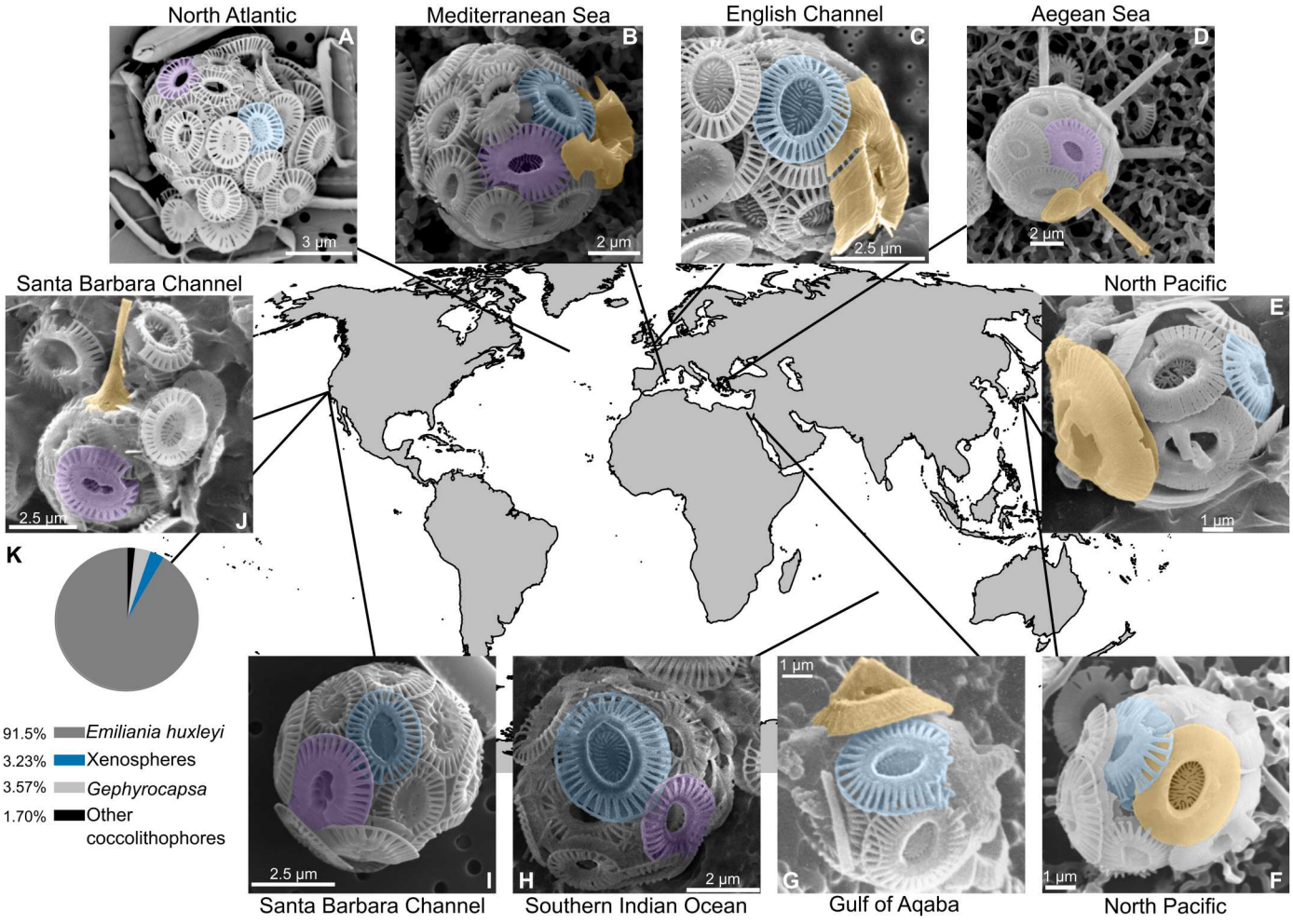

Fig. 1. Xenospheres of coccolithophores are globally distributed across diverse oceanic regions. Scanning electron microscopy (SEM) images of xenospheres composed of: (**A**) Two different *Emiliania huxleyi* coccolith morphotypes in the Northeast Atlantic [North Atlantic Virus Infection of Coccolithophores Expedition (NA-VICE); www.bco-dmo.org/project/2136]; (**B**) two different *E. huxleyi* coccolith morphotypes and a coccolith from another coccolithophore species (possibly *G. oceanica*) observed in the Mediterranean Sea (courtesy of B. D'Amario) (*18*); (**C**) *E. huxleyi* coccoliths and a coccolith from *S. corolla* observed in English Channel (courtesy of A. Taylor); (**D**) *E. huxleyi* coccoliths and coccoliths from *R. clavigera* observed in the North Aegean Sea (courtesy of M. Dimiza and O. Archontikis) (*30*); (**E** and **F**) *E. huxleyi* coccoliths and coccoliths from *Gephyrocapsa* collected from Uranouchi Bay, Kochi Prefecture, Japan [courtesy of the Electronic Microfossil Image Database System (www.emidas.org/) and K. Hagino] (*31*); (**G**) *E. huxleyi* coccoliths and a coccolith from *G. oceanica* in the Gulf of Aqaba (*21*); (**H**) two different *E. huxleyi* coccolith morphotypes collected during the fourth Indian Southern Ocean expedition (*23*); and (**I**) two different *E. huxleyi* coccolith morphotypes and (**J**) *E. huxleyi* coccoliths and a coccolith from *D. tubifera*, both observed in the Santa Barbara Channel (images from P. Matson). (**K**) Relative distribution of xenospheres (blue) compared to *E. huxleyi* (gray), *G. oceanica* (light gray), and other coccolithophore species (black) with uniform, homogenous coccospheres ($n = 1178$). Images from both (I) and (J) as well as data in (K) were derived from surface populations across all stations of the 2014 Plumes and Blooms cruise (www.oceancolor.ucsb.edu/plumes_and_blooms). (A to J) Color shading for all SEM images designates *E. huxleyi* type A morphotype (blue), other *E. huxleyi* morphotypes (type O and type OA; purple), and coccoliths from other coccolithophore species (orange). Scale bars are provided for size reference.

adsorption and support a concept of coccoliths as exchangeable elements in the environment.

We further analyzed SEM images of coccolithophore cells from an extensive dataset (n = 1178) in the Santa Barbara Channel as part of the "Plumes and Blooms" program (see Methods) to better quantify the prevalence of xenospheres in surface waters (~upper 1 m) across multiple stations in a natural coccolithophore population (*33*). Most of the coccolithophore community was composed of typical *E. huxleyi* cells with homogenous coccospheres of a single morphotype, but xenospheres were found in 75% of sampled stations and made up ~3.23% of all coccospheres; this percentage was only slightly lower than the representation of homogenous coccospheres of *Gephyrocapsa* spp. (3.57%; Fig. 1K) but higher than other coccolithophore species combined (1.70%). Other coccolithophore species included *Cyrtosphaera* spp., *Syracosphaera* spp., *Calcidiscus leptoporus*, *D. tubifera*, and *Umbellosphaera tenuis*, among others. Most of the xenospheres were made up of *E. huxleyi* coccospheres composed of more than one morphotype (Fig. 1, A, B, H, and I); others were composed of multispecies xenospheres on *E. huxleyi* type A cells (Fig. 1, B to G and J) (*7*). We found little evidence (i.e., 20 observations of "other coccolithophore" species, making up to 1.70% of 1178 observed cells; Fig. 1K) of xenospheres on other species, suggesting that *E. huxleyi* may have been particularly prone to xenosphere formation due to its widespread abundance (*34*) and the high likelihood of encounters between cells and free coccoliths within blooms. We point out that, given only one side of the cell could be visualized, the true xenosphere frequency may be underestimated in our data. Consequently, the presence of xenospheres is likely underreported because of researchers not explicitly looking for them in environmental datasets.

Multiple lines of evidence suggest that xenospheres are unlikely to be the result of SEM sample preparation (i.e., via filtration of water samples). First, xenoliths (coccoliths of foreign origin) were always incorporated in the correct orientation, with the proximal surface toward the cell and had an interlocking morphology, making these observations more consistent with biological organization. This is not always observed in SEMs of filtered free coccoliths; many are oriented with the proximal surface facing up (fig. S1). Second, the presence of different *E. huxleyi*–derived coccolith morphologies within xenospheres was likely not due to pH-induced, selective dissolution of certain biomineral morphologies, given that rinsing was done with buffered media and dissolution processes would have affected all coccoliths equally. Calcite dissolution would not provide a mechanism for the incorporation of different types of coccoliths (especially those deriving from other coccolithophore species) into *E. huxleyi* coccospheres. Third, we present extensive and multifaceted data , which derives from several independent techniques, that show adsorption occurs consistently and independently of filtering procedures within and across coccolithophore species; hence, coccolith exchange is biologically driven and is likely common in the environment. As with combination coccospheres made up of both hetero- and holococcoliths (characteristic of haploid/diploid life cycle changes) (*35*), which were initially met with some speculation in regard to their origin (*22*, *35*), coccolith xenospheres provide unexpected new insights into the biology of coccolithophores.

Free coccoliths alter the calcification state of naked *E. huxleyi cells*

We characterized coccolith adsorption dynamics and the mechanism(s) underlying these interactions using an *E. huxleyi*–based experimental system, composed of both noncalcified ("naked") and calcified cells. These two phenotypes of *E. huxleyi* occur in nature, with the former comprising about 10% of the total population (*36*); this proportion increases as cells shed coccoliths (*5*, *26*). We hypothesized that naked *E. huxleyi* cells would readily adsorb free coccoliths from the surrounding milieu. To test this hypothesis, we exposed stably noncalcifying CCMP374 cells to free coccoliths isolated and purified from a separate, stably calcifying phenotype of CCMP374 (see Methods) (*37*). The free coccolith:cell ratio ranged from ~10:1, as seen in cultures (*13*), and to 100:1, as seen in natural populations (*12*, *15*). We observed rapid coccolith adsorption (Fig. 2A) upon exposure of naked cells to 100:1 coccolith:cell using flow cytometry side scatter (SSC), a canonical proxy for the calcification state of cell populations (*5*, *11*). The presence of cells with higher SSC was diagnostic of the appearance of calcified cells via adsorption of free coccoliths. This process happened within 24 to 48 hours after coccolith addition, sometimes with more than 50% of the population becoming calcified and plateauing after 48 hours of exposure to free coccoliths (Fig. 2A and fig. S2). SEM images confirmed the adsorption and attachment of coccoliths to the cell surface (Fig. 2B). We also directly observed the adsorption and incorporation of a free coccolith into a newly scaffolded coccosphere via time-lapse microscopy (movie S1). General additive mixed modeling (GAMM), which is routinely used to model nested data (i.e., datasets with repeated measures) and to correct for temporal and spatial resolution, confirmed statistically significant differences between cell-only controls and cells exposed to free coccoliths after 96 hours (GAMM; naked cells: P value of 0.616 and naked cells + coccoliths: P value of $<2 \times 10^{-16}$; Fig. 2A; fig. S3, A and B; and tables S1 and S2).

We confirmed that the enhanced SSC was due to the adsorption of free, external coccoliths and not due to the induction of cellular recalcification of the naked cells by using coccoliths prestained with calcein, coupled with flow cytometry and confocal fluorescence microscopy. Calcein is a relatively stable, metallofluorescent dye that binds to the calcium cations within the calcite biomineral and has been routinely used to interrogate calcified structures of marine organisms (*38*). After confirming the efficient incorporation of the dye into free coccoliths (fig. S4, A to D), calcein-labeled coccoliths were added to cells at a coccolith:cell ratio of 100:1. We observed a similar dynamic and statistically significant degree of coccolith adsorption onto cells after 24 to 48 hours (GAMM; naked cells: P value of 0.835; naked cells + coccoliths: P value of 5.09×10^{-10}; Fig. 2C; fig. S3, C and D; and tables S1 and S2). Confocal microscopy showed evidence of nearly complete, fluorescently labeled coccospheres (Fig. 2D) with flow cytometry detecting as high as 60.5% calcified cells (green positive) via adsorption after 48 hours. Calcein-labeled cells had SSC signatures consistent with those of calcified populations (fig. S4, E and F).

We noted a drop in the average percentage of calcified cells (in both SSC and calcein fluorescence) (Fig. 2, A and C) from 48 to 96 hours. Given that we observed consistent removal of free coccoliths from solution over the entire time period, these reductions were not due to cells losing/shedding coccoliths. Rather, we attribute this drop to a dilution of the cellular coccolith quota during

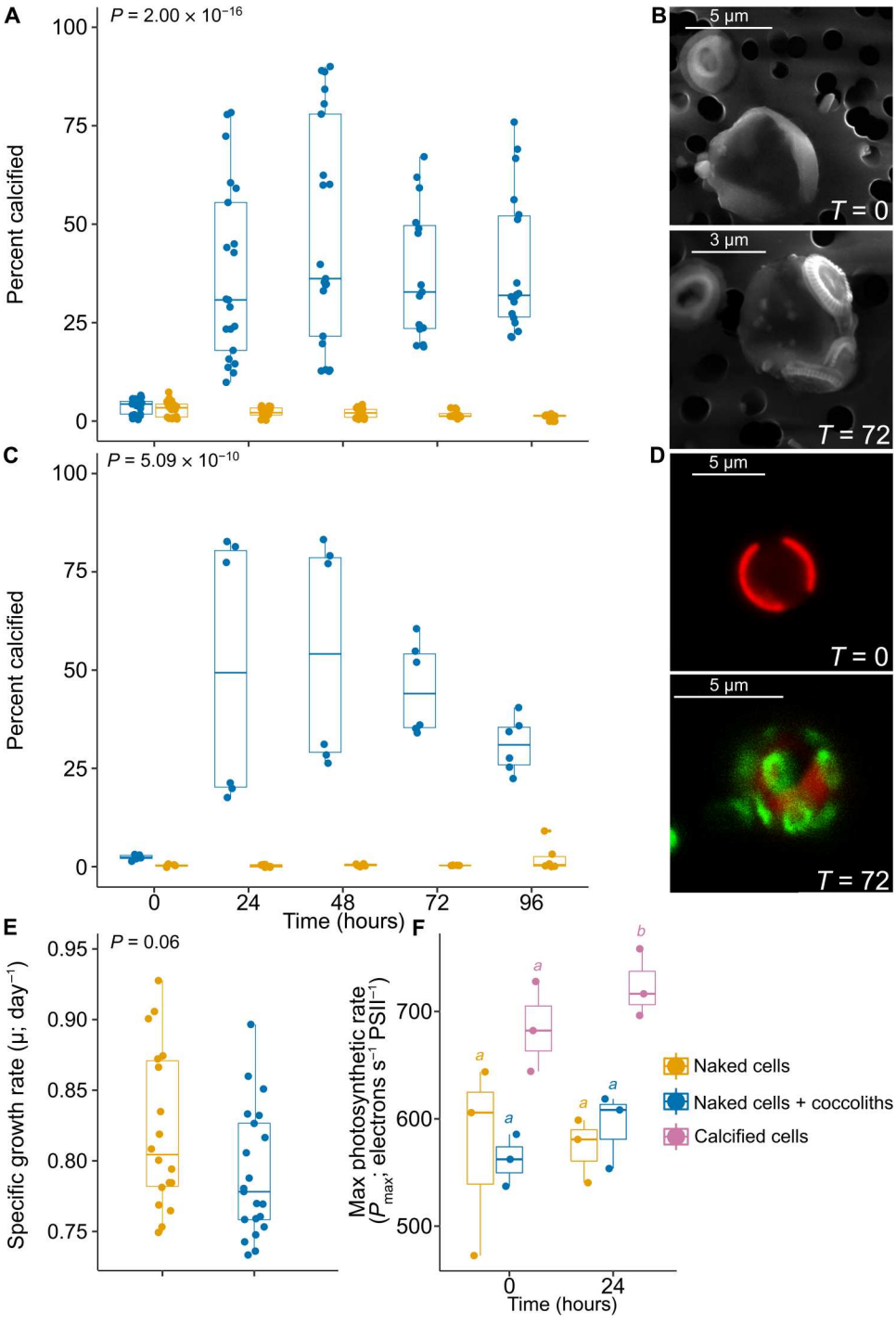

Fig. 2. *E. huxleyi* cells readily adsorb free coccoliths. Adsorption of free coccoliths to naked *E. huxleyi* cells was confirmed using flow cytometry (**A** and **C**), SEM (**B**), and fluorescence confocal microscopy (**D**). The dynamics of coccolith adsorption and the percentage of "calcified cells" were quantified using both (A) SSC, a proxy for calcification state, and (C) cell fluorescence (520 ± 15 nm) from coccoliths prestained with calcein (see Methods). Statistical significance in (A) was determined via general additive mixed modeling (GAMM; naked cells: *P* value of 0.616 and naked cells + coccoliths: *P* value of $<2 \times 10^{-16}$; fig. S3, A and B) for data over 96 hours from five pooled experiments, each containing biological triplicates ($n = 94$). Statistical significance in (C) was determined via GAMM (naked cells: *P* value of 0.835 ; naked cells + coccoliths: *P* value of 5.09×10^{-10}; fig. S3, C and D) of pooled data over 96 hours from two experiments each containing biological triplicates ($n = 6$ at each time point for each treatment). Corresponding SEM (B) and confocal (D) microscopic images confirmed coccolith adsorption to cells 72 hours after coccolith addition. For (D), red represents chlorophyll fluorescence via chloroplasts and green represents calcein-stained coccoliths. (**E**) Specific growth rates (µ; day^{-1}) of naked cells ($n = 18$) and cells with adsorbed coccoliths were indistinguishable (Mann-Whitney; $n = 21$; $P = 0.06$). Growth rates were pooled from five different experiments and correspond to cells presented in Fig. 1A. (**F**) Maximum photosynthetic rates (P_{max}) for naked cells, cells with adsorbed coccoliths, and stably calcified cells; ($n = 3$) at 0 and 24 hours after coccolith addition. Letters denote statistically significant groups as determined via one-way analysis of variance (ANOVA) and Tukey's post hoc test. For the box and whisker plots in (A), (C), (E), and (F), each point represents an individual biological replicate.

growth and partitioning among daughter cells across the population. Redistribution of coccoliths among daughter cells during division may have outpaced their ability to adsorb additional coccoliths, which is necessary for adequate detection via flow cytometry (see next paragraph). Both SSC and calcein methods captured notable variation in the degree of coccolith adsorption across different experiments, which used different batches of isolated coccoliths. This variation likely stems from varying degrees of organic matter associated with the coccoliths and possible impacts to the coccolith baseplate during isolation. This is supported by evidence that organic matter is essential to the adsorption process (See section entitled "Adsorption is mediated by coccolith-associated organic matter" below).

Confocal microscopy enabled more sensitive detection of coccolith adsorption compared to either flow cytometry method (SSC or calcein labeling). Coccolith attachment was detected as early as ~4 hours after addition with confocal microscopy, and complete coccosphere coverage was visualized by 48 to 72 hours (fig. S5).

Microscopic examination of >300 individual naked cells showed that ~53% of the population had adsorbed at least one coccolith by 48 hours compared to 21.8 and 26.8% of the population having discernible calcification signatures via SSC and calcein staining, respectively (fig. S6). These respective flow cytometry percentages rose to 32.5 and 36.9% after 72 hours, with confocal percentages remaining mostly unchanged. This analysis revealed a detection threshold associated with flow cytometry, whereby a minimum number of coccoliths must be adsorbed to generate a sufficient integrated SSC or fluorescence signal, and, hence, underestimating the number of naked cells that had actually adsorbed coccoliths. The higher sensitivity of confocal microscopy verified that inherently calcified cells adsorb calcein-stained coccoliths and incorporate them into coccospheres. At least 12.5% of these cells incorporated at least one fluorescently labeled coccolith after 24 hours (302 cells examined by confocal microscopy; fig. S7) when exposed to fluorescently labeled coccoliths at a coccolith:cell ratio of 20:1; furthermore, 2% of calcein-positive cells were detected using flow cytometry, arguing that inherently calcified cells had adsorbed a sufficient load of calcein-stained coccoliths to produce a discernable signal.

Coccolith exchange was further demonstrated within mixed assemblages of naked and calcified cells by differentially labeling cells with CellTracker Green (CTG), a fluorescent dye that is retained within living cells, transferred to daughter cells over multiple cell divisions, but is not transferred to adjacent cells in a population. Naked CCMP374 cells were stained with CTG (fig. S8A) and showed highly efficient uptake of CTG, with ~99% of the population staining positive (fig. S8B). CTG-stained naked cells were then mixed with calcified CCMP374 cells at relevant percentages found in nature (27.4% naked and 70.2% calcified; fig. S8C, top left) (*36*) and followed over a 72-hour time course. We note that only free coccoliths deriving from calcified cultures were present in the system; no additional free coccoliths were exogenously added. After 72 hours, the calcified population increased to 91.7%, 14% deriving from the starting, CTG-labeled, naked cell population. To rule out the induction of recalcification in naked cells due to dissolved elicitors, we also suspended naked cells in 0.02-μm filtered media, which derived from healthy calcifying cells; no change in the calcification state was observed. Induction of calcification by nutrient stress is also highly unlikely in this system (e.g., replete f/2 nutrients; see Methods) and within the time scale of this experiment. Together, these results confirm coccolith exchange among mixed assemblages of calcified and naked cells and argue that it is plausible in natural populations.

We also examined the extent of coccolith adsorption across other noncalcifying haptophyte species and *E. huxleyi* strains, which would be present in a mixed population. Adsorption was found to be species-specific among other noncalcified haptophytes, as only naked *E. huxleyi* cells adsorbed free coccoliths; it was not strain specific among *E. huxleyi*, as another naked strain (CCMP1516) adsorbed coccoliths derived from calcified *E. huxleyi* strain CCMP374. For example, significant adsorption (31.3% by 96 hours) of coccoliths derived from calcified CCMP374 was observed with a naked strain of *E. huxleyi* CCMP1516 (fig. S9A) (*5*, *39*). In contrast, no detectable coccolith adsorption was observed for closely related noncalcified haptophyte species *Isochrysis galbana*, *Tisochrysis lutea*, and *Phaeocystis globosa*, the latter known for producing sticky mucous on its surface (*40*). These findings argue that adsorption derives from specific cell-mineral–organic matter interactions, which require further characterization.

Given that we observed xenospheres composed of coccoliths from different species (Fig. 1) and empirically showed coccolith adsorption to calcified *E. huxleyi* cells (fig. S7), we tested whether *E. huxleyi*–derived coccoliths could adsorb to *Gephyrocapsa oceanica*, a closely related, calcifying haptophyte species. Multiple xenospheres of *G. oceanica* were observed in confocal images with ~7.95% of the population (n = 327) having incorporated at least one calcein-labeled, *E. huxleyi*–derived coccolith into the coccosphere after 24 hours of exposure (fig. S9, B and C). These results provide empirical support for the aforementioned xenospheres composed of both *E. huxleyi* and *Gephyrocapsa* spp. coccoliths (Fig. 1, E to G). They also suggest that coccolith adsorption and xenosphere formation may be more broadly shared among calcified haptophytes. A more comprehensive survey across diverse coccolithophore species is required to confidently verify.

Coccolith adsorption imparted no discernable impact on *E. huxleyi* cell physiology. Specific growth rates averaged 0.79 day^{-1} compared to 0.82 day^{-1} for naked cell-only controls (Fig. 2E). Moreover, cells with adsorbed coccoliths showed very low levels of intracellular reactive oxygen species (ROS) and nitric oxide (NO), indicating that cells were growing exponentially (fig. S10, A and B) (*39*). These cell populations had low proportions of dead cells, well below the median value (4.5%) of published percentages for exponentially growing cells (fig. S10C) (*39*). We also tested whether coccolith adsorption affected cell photochemistry at the experimental growth irradiances (150 μmol photons m^{-2} s^{-1}). Higher maximum photosynthetic rates (P_{max}) have been reported for calcified cells (*41*). Consistent with this, we observed a significantly higher P_{max} for calcifying cells compared to naked controls and cells with adsorbed coccoliths at 24 hours (723.8 versus 573.4 and 593.5 electrons s^{-1} photosystem II $(PSII)^{-1}$, respectively). P_{max} for naked cells and cells with adsorbed coccoliths were indistinguishable at 24 hours (Fig. 2F and tables S1 and S3). Statistically similar values were also observed for the slope of the Photosynthesis-Iradiance (PI) curve (α), the light saturation irradiance (E_k), and the functional absorption cross section (σ; fig. S11, A to C). We infer from these results that cells neither gained a photochemical benefit nor suffered a physiological cost by exogenously adsorbing coccoliths. It is unclear whether coccolith adsorption confers any other physiological benefit to cells. The cellular and physiological costs and benefits are still not well understood (*42*).

Adsorption is mediated by coccolith-associated organic matter

We hypothesized that the coccolith adsorption was critically mediated by coccolith-associated organic matter. Proteins and polysaccharides are known to regulate crystal growth inside the CV, a process that starts with the formation of the organic baseplate (*43*), the scaffold upon which crystal nucleation and growth occur (*44*), and the ventral surface that contacts the cell surface upon extrusion. Mature coccoliths are also coated in an organic matrix (*45*, *46*), within which coccolith-associated polysaccharides are thought to play a role in coccosphere formation and organization (*46*). We treated purified coccoliths with 10% hypochlorite to oxidize surface organics while leaving an intact crystalline structure. Hypochlorite treatment is commonly used to remove organics for

paleoceanography-related analyses of microfossils (*46*, *47*). High-resolution SEM analysis showed that the oxidation treatment effectively removed surface organics from coccoliths, including the organic baseplate (Fig. 3, A to F). Oxidized coccoliths showed little to no attachment after 24 hours across two independent experiments, with an average of 4.58% calcified cells (Fig. 3G); in contrast, untreated coccoliths showed an average of 40.7% calcified cells 24 hours after coccolith addition. While the degree of adsorption showed some variability between experiments (likely due to different batches of purified coccoliths), statistical analysis (Kruskal-Wallis with post hoc Dunn's test and Bonferroni *P* value adjustment) confirmed that populations of cells exposed to untreated coccoliths were statistically different from both naked cells and cells exposed to oxidized coccoliths (*P* values of 2.47×10^{-4} and 1.30×10^{-2}, respectively; table S4). In contrast, populations of naked cells and those exposed to oxidized coccoliths were statistically indistinguishable (*P* value of 1.00; Fig. 3G and tables S1 and S4). The coccolith organic baseplate normally covers the central area of the proximal surface (highlighted in Fig. 3, C and E, by the white arrows and dashed oval). Gaps in the calcite where the baseplate is absent are visible for coccoliths subjected to the oxidation treatment (highlighted by the white arrows and dashed ovals in Fig. 3, D and F). These results suggest that coccolith-associated organic matter, especially the organic baseplate, help facilitate the attachment of coccoliths to the cell surface.

Given the prevalence of multimorphotype *E. huxleyi* xenospheres in the environment (Fig. 1), we also tested the adsorption dynamics of different coccolith morphotypes. Not only are different morphotypes present in natural coccolithophore assemblages (*32*, *48*), but they also likely have compositional differences in coccolith-associated organics, which are implicated in determining morphology (*44*). We isolated free coccoliths from four different *E. huxleyi* strains originating from the Santa Barbara Channel such as type A, type OA, type R, and type O (fig. S12A) and added them to naked CCMP374 cells at a 100:1 coccolith:cell ratio. Coccoliths isolated from *G. oceanica* were also tested, given environmental

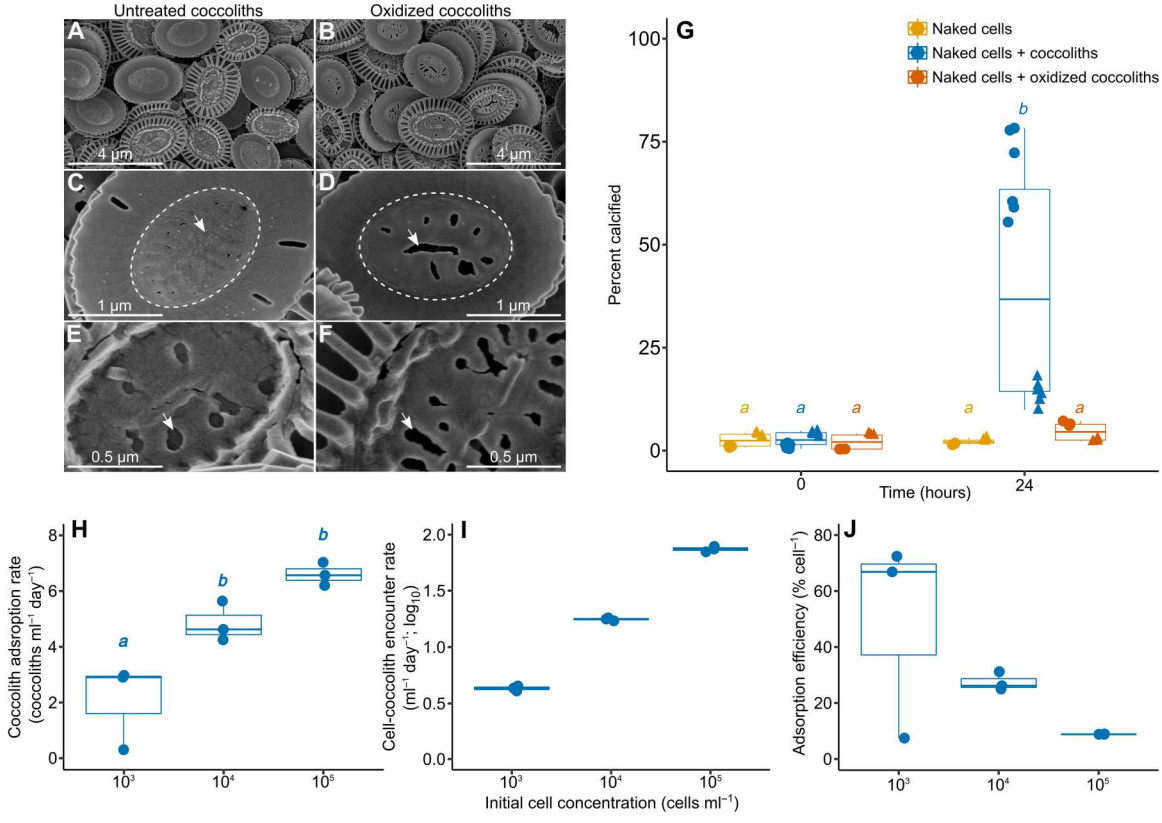

Fig. 3. Coccolith adsorption requires organic matter and is most efficient at open ocean cell concentrations. (**A** to **F**) SEM images visualizing the surface ultrastructure of untreated and oxidized coccoliths. (C) to (F) show the impact of oxidation on the organic baseplate, which makes direct contact to the cell [dashed ovals show the area of the organic baseplate on the proximal side of the coccoliths (C and D); white arrows highlight the visual differences in organic baseplate integrity between the two treatments]. Hypochlorite oxidation removed the surface organic baseplate. Scale bars are provided in each panel [magnification: (A) and (B), ×12,000; (C) and (D), ×50,000; and (E) and (F), ×100,000). (**G**) Box and whisker plot showing the impact of organic matter oxidization on coccolith adsorption after 24 hours (percentage of calcified cells using flow cytometry SSC). Oxidized coccoliths (orange; see Methods) are compared to naked cells alone (yellow) and naked cells exposed to untreated, intact coccoliths (blue). Symbols denote different experiments (each performed with biological triplicates; $n = 6$ total points, across two experiments). (**H** to **J**) Box and whisker plots of (H) measured coccolith adsorption rates (coccoliths ml^{-1} day^{-1}), (I) predicted coccolith encounter rates with cells (cell-coccolith encounters ml^{-1} day^{-1}), and (J) coccolith adsorption efficiencies for different host concentrations (ratio of the adsorption rate to the encounter rate, converted to percent per cell; see Methods for more details). Data derived from biological replicates ($n = 3$) 24 hours after coccolith addition across a range of cell concentrations and coccolith:cell ratios, including natural open ocean bloom concentrations (e.g., 10^3 cells ml^{-1} and 100:1 coccolith:cell ratio). Letters represent statistically distinct groups, as determined by Kruskal-Wallis rank sum test and a post hoc Dunn test with Bonferroni *P* value adjustment (G) and one-way ANOVA and Tukey's post hoc (H).

xenospheres were observed to contain *G. oceanica* coccoliths (Fig. 1, B, E, F, and G). Type A showed the highest attachment of all morphotypes 48 hours after coccolith addition with an average of 46.3% calcified (fig. S12, B and C); note that CCMP374 coccoliths are also type A and had a similar degree of adsorption when compared to the Santa Barbara Channel type A isolate (47.6% after 48 hours; Fig. 2A and fig. S12C). Adsorption of type OA and type R occurred at a lesser extent, averaging 24.7 and 24.2% of calcified cells, respectively (fig. S12, B and C). *G. oceanica* showed detectable, albeit lower, attachment over this time frame (~7.73% calcified cells after 48 hours; fig. S12, B and C); it increased to 13.9% calcified cells after 72 hours. Type O showed little to no attachment (1.50% after 48 hours; fig. S12, B and C); it was almost as low as naked cells alone (0.64%) and was statistically indistinguishable (Kruskal-Wallis; *P* value of 1.00; tables S1 and S4). SEM analysis confirmed the lack of attachment with this morphotype; no cells could be found with adsorbed coccoliths. The lack of adsorption is consistent with the type O morphotype having a hollow central area, lacking calcite and a visible organic baseplate (*8*). It is unlikely that type O coccoliths develop without an organic baseplate due to its importance in facilitating mineralization within the CV (*37*). However, type O coccoliths are routinely observed to be lacking organics associated with the central area (*8*), perhaps due to increased fragility of the baseplate and the lack of calcite acting to support its structural integrity in this region.

We determined the efficiency of coccolith adsorption onto cells by comparing measured removal rates with modeled encounter rates over 24 hours across a range of environmentally relevant host concentrations and coccolith:cell ratios (see Methods). Although free coccoliths adsorb to calcified cells (fig. S7), we used naked cells here because they provided a clean system. It eliminated the confounding dynamics of simultaneous coccolith production/shedding from calcified phenotypes and thereby allowed for an accurate determination of coccolith adsorption kinetics. Coccolith adsorption was observed across all treatments; adsorption rates ranged from 0.32 to 7.02 coccoliths ml^{-1} day^{-1} across concentrations of 10^3 to 10^5 cells ml^{-1} (Fig. 3H), and the adsorption rate generally scaled with increased cell and coccolith concentrations (incubations used the same coccolith:cell ratio so the number of free coccoliths scaled with the cell concentration). Cells grown between 10^4 and 10^5 cells ml^{-1} had statistically similar adsorption rates, while 10^3 cells ml^{-1} adsorbed significantly fewer coccoliths $cell^{-1}$ day^{-1} (table S3). Modeled encounter rates ranged from 4 to 79 cellsencountering coccolith ml^{-1} day^{-1} across the same cell concentrations (Fig. 3I), yielding average adsorption efficiencies of 48.9, 27.5, and 8.86% $cell^{-1}$ for 10^3, 10^4, and 10^5 cells ml^{-1}, respectively. The highest

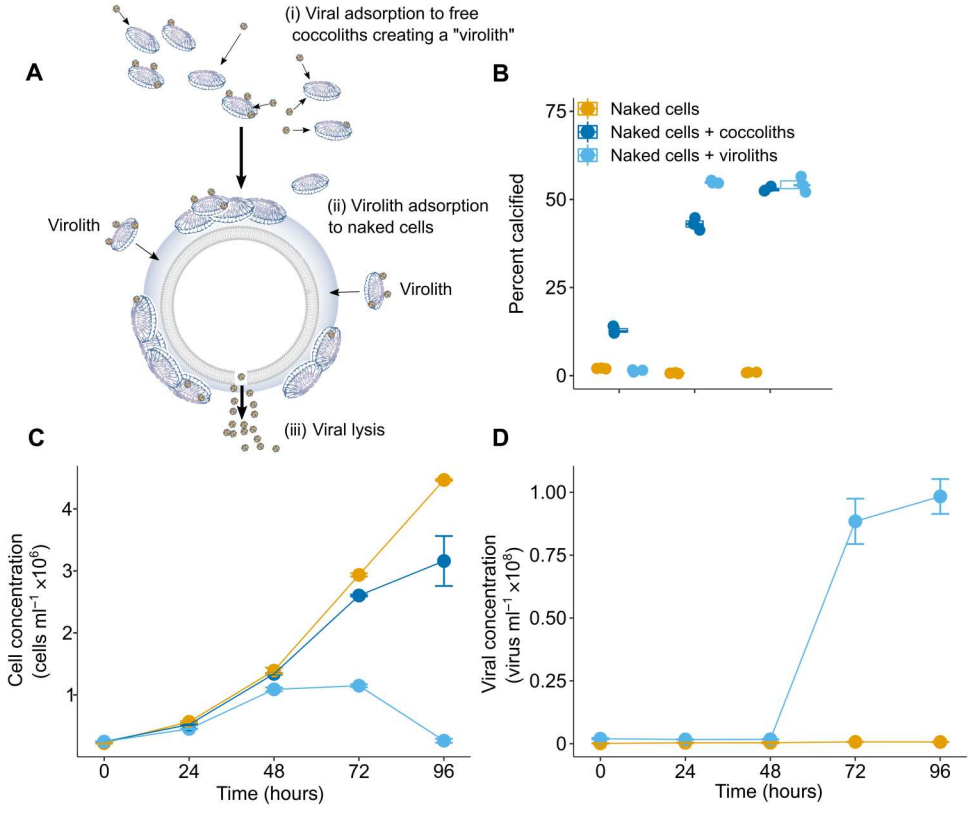

Fig. 4. Viroliths can successfully infect cells. (**A**) A conceptual model showing the facilitation of infection through coccolith adsorption: (i) virus adsorption to coccoliths and production of viroliths; (ii) virolith adsorption to cells and delivery of EhVs to the cell surface; and (iii) viral production and lysis of host cells. (**B**) Box and whisker plot showing the adsorption of untreated coccoliths (blue) and viroliths (light blue; see Methods) to cells after 48 hours compared to naked cells alone (yellow), expressed as the percentage of calcified cells using flow cytometry SSC. Points denote biological replicates (n = 3). (**C** and **D**) Time course of *E. huxleyi* cell (C) and EhV virus (D) concentrations for samples in which untreated coccoliths (blue; cell concentration only) and viroliths (light blue) were exposed to naked *E. huxleyi* cells, compared to cells only (yellow). Error bars represent the standard error across biological replicates (n = 3). Note that viroliths killed cells and had virus production after 96 hours, while supernatants containing deadsorbed, free viruses did not (fig. S14). Results confirm that viroliths effectively transmit and facilitate successful infection.

adsorption efficiency (48.9%) was observed at cell concentrations most similar to open ocean blooms (10^3 cells ml^{-1}; Fig. 3J) (28). The inverse relationship between adsorption efficiency and concentration points to a potential bottleneck in coccolith adsorption. One constraint is the cell surface area for adsorption, which will be more limiting at higher coccolith encounter and adsorption rates. Another constraint independent of cell concentration is the coccolith orientation when it contacts the cell surface. Coccoliths must encounter the cell with the proximal surface, where the organic baseplate facilitates attachment (Fig. 3, A to G, and movie S1). Given that coccoliths are secreted from a specific area of the cell (the polar end) during production (*1*), contact at this area on the cell surface may be required for adsorption. These constraints would work in concert to limit the number of encounters that can lead to successful adsorption.

Coccoliths increase host-virus encounters and facilitate infection

In light of our previous work showing that free coccoliths are highly adsorptive surfaces for Coccolithoviruses (EhVs) (*5*), we postulated that cell-coccolith interactions could facilitate virus delivery to cells and catalyze lytic infection in natural populations. EhVs lose infectivity in the environment within ~3 days (28), constraining the time window when host-virus encounters are likely to produce a successful infection. Even at low Reynolds numbers, particles contact one another at higher rates if they have higher relative velocities. We reasoned that hosts would encounter more viruses as "viroliths" (viruses adsorbed to the biomineral; Fig. 4A) than as free viruses, because viroliths are much larger than viruses and have higher encounter rates via differential settling and turbulence. Settling is unidirectional with speeds differing among particle types, whereas turbulence and Brownian motion induce random motions. All three mechanisms (turbulence, differential settling, and Brownian motion) lead to physical encounters by causing particles to move relative to one another. Although infection studies usually consider only Brownian motion, turbulence is more relevant to encounters in the ocean. Brownian motion dominates encounters of particles <1 μm in diameter (i.e., viruses contacting viruses) but becomes negligible for larger particles and in stronger turbulence with greater velocities. This transition (and turbulence generally) has been ignored in considering host-virus interactions but is well known from planktonic predator-prey and coagulation literature (*49*, *50*).

We calculated encounter rates between different entities (calcified cells, naked cells, coccoliths, and viruses) across realistic environmental concentrations (*20*, *36*) and end-member dissipation rates of turbulent kinetic energy (i.e., calm and stormy conditions; see Methods). Using published, refined sinking rates of free *E. huxleyi* coccoliths (0.205 m day^{-1}) (*51*), we estimated that a free coccolith would encounter 0.17 and 0.58 free viruses day^{-1} under calm to stormy conditions, respectively (fig. S13, A and B). Assuming 100% viral adsorption (i.e., meaning that every coccolith-virus encounter is successful), the virolith formation rates (VFRs) (% coccoliths becoming viroliths day^{-1}) would be ~17 to 58% day^{-1} across calm and stormy conditions. These VFRs do not account for coccolith production or loss but provide an estimate of the percentage of coccoliths that could be viroliths at any given time.

Cells can contact viruses by encountering viroliths or free viruses, so we hypothesized that there would be a transition point at which viroliths would be the dominant mode of virus transmission. We used the calculated encounter rates (fig. S13, A and B) to estimate the minimum fraction of coccoliths that must have adsorbed viruses [i.e., minimum fraction of viroliths (X); Eq. 14; see Methods] for more of the infection to be transmitted by viroliths than by free viruses. When the daily virolith fraction (VF) is higher than X (i.e., VF > X), the dominant mode of infection would be transmission via viroliths. Our calculations show that calcified cells would require a minimum of X = 100% and 22% in calm and stormy conditions, respectively, while naked cells would require a minimum X = 39% and 17% (fig. S13. A and B). If we assume that the fraction of viroliths is equivalent to the VFR given above, then these estimates of X suggest that free viruses are the dominant mode of infection in calm conditions and viroliths in stormy conditions, with transition points at intermediate turbulence (between 10^{-4} and 10^{-5} m^2 s^{-3} for naked cells and ~10^{-4} m^2 s^{-3} for calcified cells, respectively; fig. S13E). These calculations contain uncertainties associated with the adsorption efficiency of viruses to coccoliths and the turnover rate of coccoliths in the mixed layer, which depends on vertical mixing and coccolith dynamics (e.g., shedding, adsorption, and dissolution rates) that are beyond the scope of this paper. Nonetheless, our estimates demonstrate that it is possible for virolith-driven infection to be the dominate mode of infection in realistic ocean turbulence.

The ability of viroliths to catalyze infection under different turbulent regimes is further supported by the shorter encounter times between cells and viroliths than between cells and free viruses. *E. huxleyi* cells would encounter a coccolith once every ~45 to 103 hours compared to a free virus every ~53 to 116 hours under calm conditions. Under strong turbulence, the encounter rates drop to ~1.5 to 2 hours for coccolith compared to ~7 to 12 hours for a free virus (fig. S13, C and D), such that even if only ~20% of coccoliths were viroliths, the encounter time would still be shorter for viroliths than for viruses. We acknowledge that our calculations are insufficient to accurately determine the relative rates at which cells become infected by free viruses versus viroliths. These rates depend, in part, on whether viruses remain infective longer when adsorbed to coccoliths. Uncertainties in both encounter rates and infectivity affect the net infection rates but are difficult to quantify, and modeling these dynamics is beyond the scope of our paper. We are actively investigating virus adsorption coefficients for coccoliths, the incorporation of differential settling in viral adsorption estimates, and the inclusion of empirical entity concentrations and dissipation rates for different oceanic regimes.

We experimentally confirmed that viroliths efficiently deliver infectious viruses to cells and expedite infection. We generated viroliths (1.02 ± 0.03 EhVs per coccolith; fig. S14A; see Methods) and exposed them to naked cells at a 50:1 ratio, simultaneously measuring coccolith adsorption and both cell and viral concentrations over a 96-hour time course (Fig. 4, B to D, and fig. S14, B to F). Respective coccolith adsorption values averaged as high as 43.0 and 54.9% for naked cells exposed to coccoliths and to viroliths, for 24 hours; both treatments reached similar percentages by 48 to 72 hours (Fig. 4B and fig. S14B). Viroliths successfully facilitated lytic EhV infection with cell growth plateauing 72 to 96 hours after addition along with concomitant spikes in viral production (Fig. 4, C and D, and fig. S14, C to F). GAMM was used to statistically compare trends between treatments (control, naked cells + coccoliths, naked cells + viroliths, and naked cells + virolith supernatant; fig. S14, E and F) and to perform pairwise comparisons (fig. S15, A

and B). Virolith exposure was the only treatment that produced a significantly different trend to other treatments, with higher cell mortality and virus production (figs. S14, E and F and S15, A and B).

We tested and confirmed that the increased cell mortality associated with the washed virolith treatments (Fig. 4 and figs. S14 and S15) was not due to higher viral loads (fig. S14A, blue and green symbols). Three independent experiments were performed across different volumes (250 µl to 40 ml; Fig. 5 and fig. S16) and further validated both our model-based predictions and conclusions of enhanced cell mortality due to virolith formation. These experiments showed that viroliths can deliver infectious viruses to cells, causing more lysis and cell death than with free viruses alone, especially at low cell-virus encounter rates. Here, a range of virus:host ratios (0.01 to 10; Fig. 5, C to F, and fig. S16, A and B) were used to simulate low and higher encounter rates between naked cells and virus. One group received viruses alone, whereas the other group received both virus and coccoliths (to form viroliths) with the only difference being the presence of coccoliths. Experiments used coccoliths derived from high-speed, fluorescence-activated cell sorting (FACS) and from bulk extraction (see Methods), two fundamentally different isolation procedures. These comparisons allowed for a rigorous assessment of whether coccolith biominerals accentuate viral infection compared to free viruses alone. While the presence of coccolith biominerals lowered infectious virus titers by 38% (6.88×10^5 infectious viruses ml^{-1} compared to 1.11×10^6 infectious viruses ml^{-1} for viruses alone; assessed via a microtiter-based, most probably, number technique; Fig. 5, A and B), viroliths consistently killed more cells after 96 to 240 hours in scenarios with low virus:host ratios (0.01, 0.1, and 1.0; see black boxes), conditions with relatively low cell-virus encounter rates (Fig. 5, C to F, and fig. S16, A and B). Infections performed with viroliths decreased cell concentrations by ~100 and 150% after 96 (fig. S16A) and 168 hours (fig. S16B) for virus:host ratios of 0.01 and 0.1, respectively; this translated into ~119,000 to 380,000 more cells per ml dying in the presence of viroliths compared to viruses alone. These differences disappeared (and even reversed; free viruses killed more cells than viroliths) at a virus:host ratio of 5 (fig. S16B), likely due to sufficiently high encounter rates between free viruses and cells at these concentrations, which negate the differential impact of viroliths.

The adsorptive exchange of coccolith biominerals has ecological and biogeochemical implications that accompany their incorporation into sinking particles (marine snow, transparent exopolymeric particles, and fecal pellets) (*19*, *20*, *52*). Coccoliths have also been observed to adsorb external, biochemically active enzymes, raising the possibility that they may even facilitate organic matter transformation within sinking aggregates (*53*). Widespread observations of xenospheres in the environment, combined with experimental evidence of organic-mediated adsorption and frequent encounters with both viruses and cells, put these biominerals at the heart of interactive arms races between coccolithophore hosts and the viruses that infect and kill them. This dynamic landscape of calcite exchange can have disparate impacts on biological interactions, depending on whether they harbor adsorbed viruses.

Coccoliths play multifaceted ecological roles

Our current findings, together with previously published work (*5*), show that coccolith biominerals can play both beneficial and antagonistic roles with respect to virus infection, and, while dynamic, these roles must be layered into our understanding of the mechanisms of infection in natural environments (Fig. 6). Coccoliths within the coccosphere can provide physical protection against viruses during early stages of infection and prevent virions from contacting the cell surface (Fig. 6, top section, blue) (*5*). They can also slightly lower the infectious titer of the virus population through their adsorptive properties [this study and (*5*)], both serving to delay infection. At the same time, viroliths can act as facilitators of infection and catalysts for death, adsorbing and delivering many more viruses to cells (via much higher encounter rates that overcome lower infectious titers; Fig. 5, A and B) for successful infection, analogous to a virulent "Trojan Horse" (Fig. 6, bottom section, pink) (*54*). We reason that this process may be accentuated in stages of infection that are characterized by massive coccolith shedding and elevated viral production, both of which would enhance virolith formation and encounter rates (*5*, *26*, *36*). Reconciling these respective roles depends on the nature of the system and the temporal dynamics. Our findings show that, despite being passive entities, planktonic calcite coccoliths play a fundamental and impactful role in biomineral-cell-virus interactions in the environment.

METHODS

Culture growth and maintenance

Naked *E. huxleyi* CCMP374 and CCMP1516 were obtained from the National Center for Marine Algae and Microbiota (https://ncma.bigelow.org). *Phaeocystis globosa* was provided by L. Karp-Boss (University of Maine), while *Gephyrocapsa oceanica* was provided by K. Wyman (Rutgers University). *I. galbana* and *T. lutea* were provided by the New Jersey Aquaculture Innovation Center at Rutgers University, courtesy of M. De Luca, S. Towers, and J. Kiernan. *P. globosa*, *G. oceanica*, *I. galbana*, *T. lutea*, and naked *E. huxleyi* strains were maintained in f/2-Si seawater-based medium (55). Calcified *E. huxleyi* CCMP374 cells were derived from a previous study (*5*). *E. huxleyi* strains with different morphotypes were isolated from the California coast (PnB271_B9_TypeA, June_4_A12_TypeR, June_4_A5_TypeOverA- isolated from the Santa Barbara Channel; MBB5_TypeO isolated from Monterey Bay) and morphotyped via SEM analysis. Calcified *E. huxleyi* cells were maintained in altered (N:P; final concentration of 100:6.24 µM) (*15*, *56*) f/2-Si media and transferred to replete f/2-Si media for coccolith isolation and experiments. Nearly all cell cultures were grown in 40-ml plastic culture flasks (CELLSTAR Cell Culture Flasks with filter cap, Greiner Bio-One) at 18°C under a 14:10 light:dark (L:D) cycle at 150 µmol photons m^{-2} s^{-1}. The only exception is *G. oceanica* cells used for calcein-labeled coccolith adsorption experiments (fig. S9B), which were grown at 5-ml volumes in 15-ml falcon tubes (Corning Inc., Corning, NY) under the same growth conditions as previously described.

Coccolith isolation and treatment

Coccolith isolation followed previously published procedures (*37*). Briefly, ~1-liter cultures of calcified *E. huxleyi* cells were grown to late exponential phase, $>1 \times 10^6$ cells ml^{-1}. Cells were collected onto 1.2-µm pore size, 47-mm diameter polycarbonate filters (Isopore, EMD Millipore) and resuspended in 7 ml of 0.22-µm filtered seawater in a 15-ml falcon tube. Cells were pelleted at speed 6 (30-cm radius, swing bucket rotor; ~3000*g*; Fisher Scientific Centrific Model 225 centrifuge) for ~20 min at room temperature. The

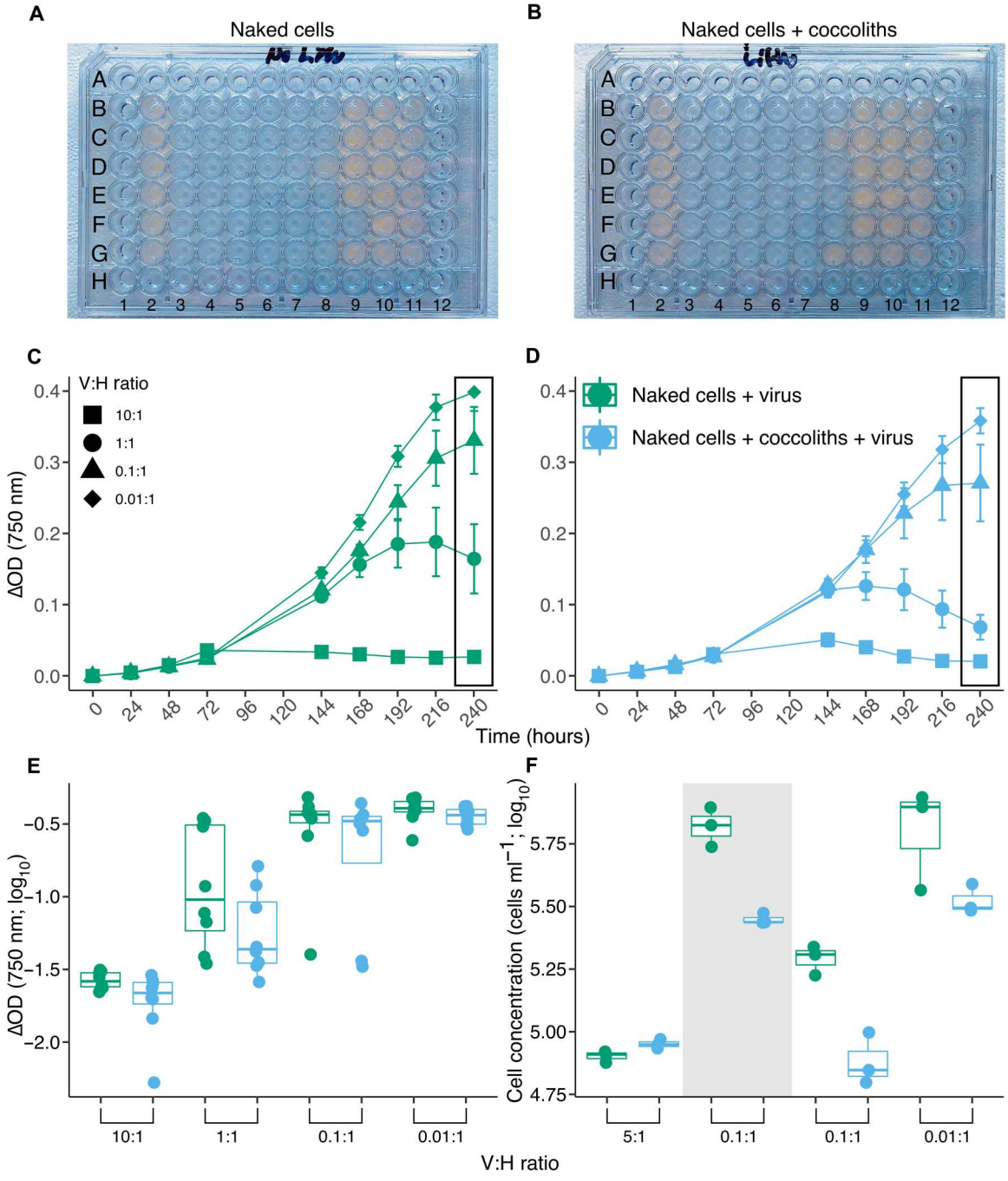

Fig. 5. Coccoliths lower infectivity but facilitate infection. Microtiter-based, most probable number assays in the absence (**A**) or presence (**B**) of coccoliths (column no. 2, uninfected controls; columns no. 3 to 11, EhV dilution series; rows B to G, technical replicates; $n = 6$). Plates were imaged after a 2-week incubation with lysis being scored to calculate respective EhV infectious titers. (**C** and **D**) Time course of small volume (250 μl) infections in the absence (C) or presence (D) of coccoliths [change in optical density (ΔOD_{750}); see Methods]. Cells were infected at different virus:host (V:H) ratios (symbols) and received 50:1 coccolith:cell (light blue) or no coccoliths (green). Error bars denote SE across technical replicates ($n = 8$). Black boxes denote time points used for detailed examination in (E). (**E**) Box and whisker plots show virus + coccolith treatments had lower average ΔOD_{750} values across V:H ratios, although not statistically significant [10:1; 1:1, and 0.1:1 (Mann-Whitney *U* test); 0.01:1 (Student's *t* test); *P* values: 6.50×10^{-2}, 1.95×10^{-1}, 1.95×10^{-1}, and 2.23×10^{-1}, respectively]. (**F**) Box and whisker plots from two, larger volume (40 ml) experiments at different V:H ratios (see time series in fig. S16). Experiments used fluorescence-activated cell sorting–sorted coccoliths (gray shading) or coccoliths isolated via density centrifugation (all other data points; see Methods). V:H ratios of 0.1 were significantly different (gray, *P* value of 5.13×10^{-3}, Student's *t* test; white background, *P* value of 3.62×10^{-3} Mann-Whitney *U* test). Data for V:H of 0.01 were visually different (non-overlapping first and third quartiles) but not statistically significant (*P* value of 0.20, Mann-Whitney *U* test). V:H ratio of 5 was weakly significant (*P* value of 4.28×10^{-2}, Student's *t* test) but had the opposite trend (i.e., viroliths killed fewer cells). Individual data points are shown and denote biological replicates ($n = 3$). Color legend (D) applies to (C) to (F), while the shape legend (C) only applies to (C) and (D).

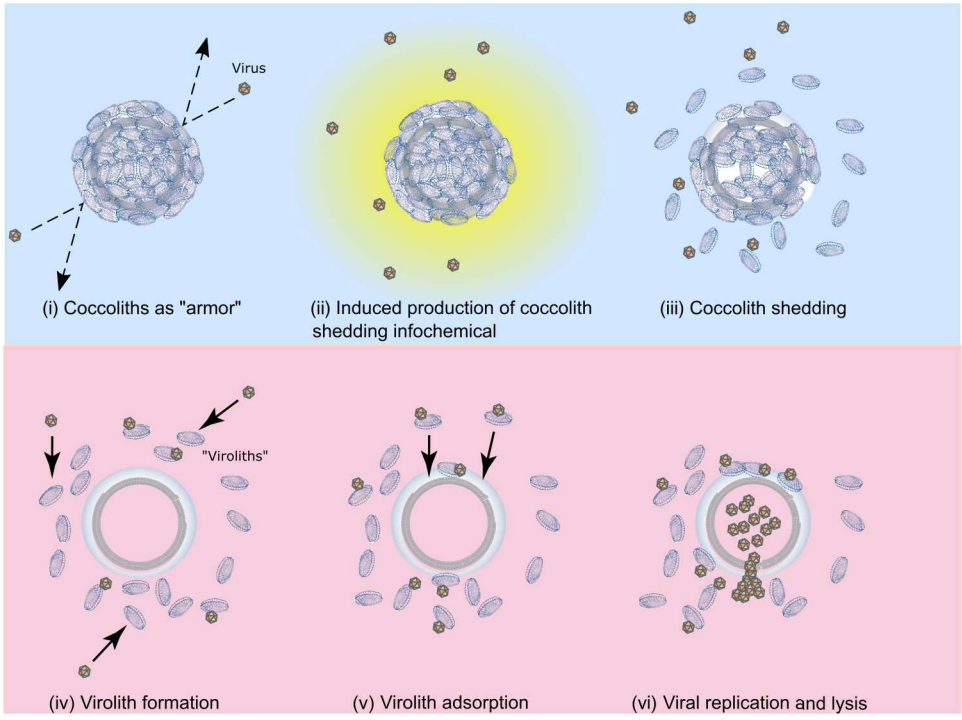

Fig. 6. The multifaceted roles of coccoliths in *E. huxleyi*–EhV interactions. A conceptual model highlighting the mulitfaceted roles of coccoliths during viral infection. The top section (i to iii; shaded blue) represents the beneficial roles of coccoliths to host cells by delaying infection as described in a previous study (*5*); the bottom section (iv to vi; shaded pink) highlights of the antagonistic roles of coccoliths to host cells by facilitating infection via viroliths as described in this study. (i) Coccoliths in an intact coccosphere can help delay infection by preventing viruses from contacting the cell surface; (ii) exposure to viruses induces the production of a host-derived, unidentifed infochemical (yellow) that triggers coccolith shedding; (iii) coccolith shedding occurs before cell lysis, increasing the concentration of naked cells and free coccoliths within a population, with the coccoliths adsorbing and removing free viruses from the surrounding milleu; (iv) virus adsorption to free coccoliths leads to the formation of viroliths; (v) virolith adsorption to cells increases the encounter rate of viruses to cells and promotes delivery of infectious EhVs to the cell surface; (vi) viral production and lysis of host cells, in conjuction with virus-induced cocolith shedding, increases the likelihood of further virolith formation.

supernatant was removed, and cells were resuspended in 1 ml of 1 M KNO_3 and transferred to 2-ml Eppendorf tubes. Cells were incubated at room temperature with gentle rocking for ~30 to 45 min. Upon removal, cell and coccolith materials were pelleted via centrifugation (as above), and KNO_3 was removed and replaced with a silica colloid, Percoll (pH 8.5 to 9.5 at 25°C; Sigma-Aldrich, P4937). Coccoliths were then isolated from organics and cell debris via density gradient centrifugation (8.2-cm radius, fixed angle rotor; ~3300*g*; Eppendorf Microcentrifuge 5415D) for ~1 min at room temperature. The supernatant and any organic debris that had collected on the side wall of the Eppendorf tubes were removed. These cleaning steps with Percoll were repeated until the supernatant was clear, devoid of greenish color, and cell debris was no longer collected on the side walls. Coccoliths were then washed three times with 1 ml of 0.22-μm filtered seawater and lastly resuspended in 1 ml of 0.22-μm filtered seawater and stored at 4°C in the dark before use. Coccoliths were quantified using a BD Influx 209S Mariner flow cytometer, as described in the "Flow cytometry analysis" section below. Before quantification, coccolith stocks were diluted 1000-fold in 0.22-μm filtered seawater.

Coccolith-associated organics were removed by incubating purified coccoliths (from above) with 0.22-μm pore size and filtered 10% hypochlorite (NaClO; v/v) for ~24 hours at room temperature with gentle rocking (*57*). After incubation, coccoliths were washed six times with 0.22-μm filtered seawater to remove residual 10% hypochlorite. Cleaned coccoliths were resuspended in 1 ml of 0.22-μm filtered seawater and then stored at 4°C in the dark prior to use. Coccolith stock concentrations were determined using flow cytometry.

Exogenous coccolith additions

Stably naked (noncalcified) cell cultures (CCMP374, CCMP1516, *I. galbana*, and *T. lutea*) were grown to cell concentrations of ~1×10^4 to 1×10^5 cells ml^{-1}. Note that, for experiments with *P. globosa* (data shown in fig. S9A), exogenous coccolith additions began at starting cell concentrations of 5.30×10^3 to 6.48×10^3. *P. globosa* cells were monitored for adsorption up to 240 hours after coccolith addition, with an additional exogenous addition at 100 hours. No detectable attachment was observed through 240 hours, and only the first 96 hours are shown.

Coccoliths were added to cells at a various coccolith:cell ratios (0.1:1, 10:1, 50:1, and 100:1; see table S1); most experiments were performed using 100:1. Experiments were performed in identical growth conditions and culturing flasks as described above. Cell concentrations, coccolith concentrations, and the percentage of calcified cells were monitored via analytical flow cytometry over a 96-hour time course. Samples were also taken for confocal microscopy, SEM, stress markers [staining to assess the physiological state of cells; reactive oxygen stress (ROS), intracellular NO, and percentage of dead cells], and photophysiological measurements at discrete

time points. Coccolith addition experiments were all done with biological triplicates.

Growth rates

The specific growth rate was determined by calculating the natural log of cell concentrations and calculating the slope over the course of the experiment (96 hours). These slopes were pooled across multiple experiments (n = 5) for two different treatments (naked cells and naked cells with coccoliths). Data were analyzed for normality before performing a Mann-Whitney U test to assess statistical significance.

Photochemical measurements

Fluorescence-based photosynthetic measurements were determined using a mini fluorescence induction and relaxation system (FIRe), using a custom-built FIRe and established protocols (*58*). Samples (5 ml)—naked cells, actively calcifying cells, or naked cells exposed to coccoliths incubated at 150 μmol photons m^{-2} s^{-1} were dark-adapted for ~10 min at 18°C and then analyzed on the FIRe using fluorescence induction at the microsecond time scale across 18 light irradiance steps ranging from 0 to 500 μmol photons m^{-2} s^{-1}. PI curves were generated by measuring electron transfer rates ($P = E \times \sigma_{PSII} \times \Delta F'/F_m'$) as a function of light irradiance (E; μmol photons m^{-2} s^{-1}). σ_{PSII} is defined as the functional absorption cross-section of PSII, ΔF is the difference in maximum and minimum fluorescence between cells exposed to light, and F_m' is the fluorescence maximum in the light. The maximum rates of photosynthetic electron transport (P_{max}) were determined by fitting the PI curves with the exponential rise function, $P = P_{max}(1 - \exp(E/E_k)$, where E_k is the light saturation irradiance.

Cell, coccolith, and virus staining

Coccoliths were fluorescently tagged using calcein {bis[*N*,*N* bis(carboxylmethyl)aminomethyl]fluorescein; C0875; Sigma-Aldrich, St. Louis, MO}, which was made into 20 mM stocks in dimethyl sulfoxide (DMSO) and stored in the dark on ice before each use. Coccolith stocks were pelleted via centrifugation, the supernatant was removed, and replaced with 1 ml of Hepes-buffered seawater. Coccoliths were resuspended and transferred to a 12-ml falcon tube containing 4 ml of Hepes-buffered seawater. Hepes-buffered seawater was necessary to offset the pH ~0.75 drop upon addition of 0.2 mM calcein to unbuffered seawater (*38*), which could compromise the coccolith structure. Coccoliths were mixed, and staining was initiated upon the addition of 50 μl of the 20 mM calcein stock. The 15-ml falcon tube was placed on a rocker and allowed incubation for ~3 hours at 4°C. Coccoliths were pelleted and washed ~6 times with 0.22-μm filtered seawater to remove the residual stain and then stored at 4°C in the dark before use. Calcein-positive coccoliths were detected via flow cytometry using 520-nm fluorescence.

Naked CCMP374 cells were stained with CTG 5-chloromethylfluorescein diacetate (Invitrogen, Thermo Fisher Scientific, Waltham, MA), a nontoxic stain that passes freely through the cell membrane, forming a cell-impermeant fluorescent compound. One millimolar stocks of CTG were made up in DMSO, and 5 ml of cell culture was stained at a final concentration of 10 μM for 60 min at growth temperature (18°C). Cells were centrifuged (30-cm radius, swing bucket rotor; ~3000*g* for 5 min; Fisher Scientific Centrific Model 225 centrifuge), and the supernatant was removed. Cells were resuspended in fresh f/2-Si media and stored at 18°C before use.

Intracellular ROS was determined using the membrane-permeable fluorescent probe, CM-H_2DCFDA (Invitrogen, Thermo Fisher Scientific, Waltham, MA), which serves as a general marker for ROS species (*39*). This probe becomes fluorescent upon cleavage of the acetate groups via intracellular esterases and oxidation by ROS. Stocks were made up to 1 mM in DMSO (Sigma-Aldrich, St. Louis, MO) and stored at −20°C until needed. Before analysis, cell samples were stained at final concentrations of 5 μM and incubated at room temperature in the dark for ~45 min. ROS-positive cells were detected via flow cytometry using median fluorescence units at 520-nm range and normalized to an unstained control to remove background fluorescence.

Intracellular NO was determined using a NO-specific membrane permeable fluorescent probe, 4-Amino-5-methylamino-2',7'-difluorofluorescein diacetate (DAF-FM-DA; Invitrogen, Thermo Fisher Scientific, Waltham, MA) (*39*). Once inside the cell, DAF-FM-DA is cleaved by intracellular esterases and accumulates within. DAF-FM-DA will fluoresce once bound to a NO molecule forming a fluorescent triazole product. Stocks (5 mM) were made up in DMSO and frozen at −20°C until use. Cells were stained at a final concentration of 5 μM and incubated in the dark for ~45 min at room temperature. Cellular NO levels were measured via flow cytometry using median fluorescence units at 520 nm and normalized to an unstained control to remove background fluorescence.

The percentage of dead cells was quantified using a cell impermeable fluorescent stain, SYTOX Green (SYTOX, Invitrogen, Thermo Fisher Scientific, Waltham, MA) (*38*). Stocks (5 mM) were stored at −20°C until use. Cells were stained at a final concentration of 1 μM and incubated in the dark for 15 min at room temperature. The percentage of dead cells was determined via flow cytometry at 520-nm fluorescence of chlorophyll-containing cells. A gate was used for a negative unstained control to define living cells. The percentage of cells above this cutoff was defined as having compromised membranes (functionally dead). Unstained controls were used to remove any background fluorescence.

Virus concentration (Fig. 4D and figs. S14D and S16D) was determined by staining with SYBR Green (Invitrogen, Thermo Fisher Scientific, Waltham, MA) and measurements of green fluorescence (520 nm, 40-nm bandpass) as previously described (*59*). A total of 100 μl of sample was fixed with glutaraldehyde (0.5% final concentration) and stored for 15 to 30 min at 4°C, followed by flash freezing in liquid nitrogen and storage at −80°C until further processing. Samples were then thawed, diluted 50-fold in 0.22-μm filtered tris/EDTA buffer (pH 8), stained with SYBR Green (0.5 to 1× final concentration), incubated for 10 min at 80°C in the dark, cooled to room temperature for 5 min, and mixed thoroughly before counting on the flow cytometer. Virus concentrations were measured using a pressure differential (between sheath and sample fluid) of 0.7, resulting in a low flow rate for optimal viral abundances.

Flow cytometry analysis

Three different flow cytometers were used in the collection of these data: BD Accuri C6, BD Influx Model 209S Mariner, and BD FACSCelesta. The BD Accuri C6 is equipped with a two-laser setup (488 and 640 nm) and four-color emission detection with user-

changeable optical filters. The BD Influx Model 209S Mariner flow cytometer high-speed cell sorter is equipped with a 488-nm, 200-mW blue laser; a four-way sort module; and two scatter, two polarized, and four fluorescence detectors. This sorter was used for both analysis and the sorting of free coccoliths (fig. S16A). Last, the BD FACSCelesta is equipped with a three-laser setup (488, 405, and 640 nm) configured for a three-color detection with interchangeable optical filters (BD Biosciences).

Both the BD Accuri C6 and BD FACSCelesta use fixed laser alignment. Quality control was performed using Spherotech 8-peak rainbow calibration particles (www.spherotech.com/CalibrationParticles.htm). The BD Influx Mariner required daily laser alignment and QC using fluorescent size calibration (3 μm) Spherotech rainbow particles and the coefficient of variation in the 520-nm signal, and forward scatter (FSC) signals were always <2%. Brewster angle optics were also used to measure depolarization of forward scatter light by cells and particles as previously described (*5*, *11*). Brewster windows were oriented so that they either transmitted FSC light with polarization parallel to the sample stream (parallel polarized FSC light) or reflected FSC light polarized orthogonal to the sample stream (orthogonally polarized FSC light), both going to individual photomultiplier detectors. This configuration was used to both quantify coccolith concentrations across experiments and to optically sort free coccoliths from calcified cells. A visual example of the flow cytometric configuration for coccolith quantification and sorting can be found in Johns *et al*. (*5*).

Across all instruments, cell concentrations were quantified using chlorophyll fluorescence (692 nm, 40-nm band pass), FCS, and SSC. Both SSC (a proxy for the degree of calcification) (*5*, *11*) and 520 ± 15–nm fluorescence (calcein fluorescence) were used for the determination of the percentage of calcified cells. Each cytometer used different collection software: BD Accuri C6 software, BD FACS software, and BD FACSDiva. However, all flow cytometric data after collection were analyzed using the program FlowJo 8.8.7 (Ashland, OR, USA).

Scanning electron microscopy

For SEM images in Fig. 1 (I, J, and K) and fig. S12A (*G. oceanica*), which derive from the Santa Barbara Channel and the Plumes and Blooms cruise (www.oceancolor.ucsb.edu/plumes_and_blooms), 500 ml of seawater was gravity settled over night and concentrated down to 50 ml. For fig. S12A (type A and type R) each sample consisted of an aliquot of 1 to 3 ml. All samples were then gently vacuum-filtered through a 13-mm, 0.4-μm pore size polycarbonate filter (Isopore, EMD Millipore). Filters were dried overnight at room temperature and stored in plastic petri slide cases. Each dried filter was affixed to a 12.7-mm aluminum pin stub using carbon adhesive tabs and sputter-coated with gold for 300 s before analyses. These samples were examined under a Zeiss EVO 40 XVP scanning electron microscope at the Santa Barbara Museum of Natural History (CA, USA). To determine the fraction of *E. huxleyi*, *Gephyrocapsa* spp., xenospheres, and other coccolithophores, the total number of each entity was divided by the total number of individual cells (n = 1178; Fig. 1K). In the SEM images shown in Fig. 2B, samples (1 ml) were vacuum-filtered onto 1.2-μm pore size polycarbonate filters (Isopore, EMD Millipore), dried for ~24 hours, and stored in a desiccator until imaged using a Phenom ProX benchtop scanning electron microscope (Phenom World). Image detection used both a high-sensitivity backscatter electron detector and a secondary electron detector. For SEM images of isolated coccoliths (CCMP374; Fig. 3, A to F, and figs. S1 and S12A), coccolith stocks were diluted 100-fold in a syringe housing and collected onto 13-mm, 0.4-μm pore size polycarbonate filters using a Swinnex housing and gentle pressure. Filters were washed with four times the volume of Hepes-buffered Mili-Q to remove salts. Filters were air-dried and mounted onto an aluminum SEM stub with carbon adhesive tabs before sputter coating with 10-nm Pt/Pd. Samples were imaged using a field-emission scanning electron microscope (FEI Verios 460L) operated by the Analytical Imaging Facility at North Carolina State University.

Confocal microscopy

For images shown in Fig. 2 and figs. S4, S5, and S7, calcein-stained coccoliths and *E. huxleyi* cells were transferred to a 35-mm coverslip petri dish (MatTek Corp. Ashland, MA, USA) and imaged using a Leica SP8 confocal microscope supported by Leica Application Suite X for acquisition and analysis. A 488-nm laser was used to excite both calcein (emission: ~520 nm) and chlorophyll (emission: ~692 nm). Both coccoliths and cells were visualized with a ×63 oil immersion lens [numerical aperture (NA) = 1.3], with the detector pinhole set to one airy disc unit, resulting in an optical thickness of 0.9 μm. For images shown in fig. S9B, 20 μl of *G. oceanica* cells incubating with calcein-stained coccoliths was removed from 15-ml falcon tubes, transferred to a microscope slide, and imaged using a Zeiss LSM 710 confocal microscope supported by Zeiss Zen Lite (v3.6) for acquisition and analysis. The same laser settings were used as described above. Cells were imaged with an ×100 oil immersion lens (NA = 1.4), with the detector pinhole set to one airy disc unit.

Time-lapse light microscopy

Noncalcified *E. huxleyi* CCMP374 cells were mixed with untreated coccoliths at a 100:1 coccolith:cell ratio and gently mixed before plating out onto a coverslip petri dish (MatTek Corp. Ashland, MA, USA) for imaging on an inverted Olympus IX 71 microscope equipped with ×100 oil immersion lens (NA = 1.3). Brightfield color images were acquired at 60-s intervals using an Infinity 3 digital color camera controlled with the manufacturer's software (Infinity Analyze 7.0, Lumenera Corp., Canada). The video was made using 5 frames/s (movie S1).

Coccolith removal and encounter rates

To quantify the rate at which coccoliths adsorb to cells (Fig. 3H), we first quantified the loss of free coccoliths by finding the slopes of the linear regressions of the ratio of free coccolith concentration to initial concentration over time (D; day^{-1}). Coccolith concentrations were measured over 96 hours. Each experiment was conducted with blank treatments, consisting of f/2-Si media with coccoliths added to experimental containers at similar concentrations to those given to cells to correct for background coccolith loss. D was calculated as

$$D = \left[\ln\left(\frac{L_t}{L_0}\right) - \ln\left(\frac{B_t}{B_0}\right)\right]/t \quad (1)$$

where L and B represent the experimental and blank treatments, respectively. L_t and B_t are the coccolith concentrations at time t, and L_0 and B_0 are the coccolith concentrations at the start of the experiment. We determined the slope of each experimental replicate and

corrected it for background adsorption by subtracting the average slope of the blanks.

Using the regression slopes D for each replicate derived from Eq. 1, we calculated the coccolith adsorption rate (A; coccoliths ml^{-1} day^{-1})

$$A = -{L_0}^* D \tag{2}$$

where the minus sign indicates that the adsorption is uptake and has a sign opposite to the loss rate measured in Eq. 1.

Theoretical encounter rates among entities (calcified cells, naked cells, coccoliths, and viruses) were calculated using

$$E = \beta C_1 C_2 \tag{3}$$

where E (encounters ml^{-1} day^{-1}) is the encounter rate, β is the encounter kernel (ml day^{-1}), and C_1 and C_2 are entity concentrations, respectively. The per-entity encounter rate is E/C_1 (fig. S13, A and B).

The kernel β dictates the initial contact rate and can only be calculated theoretically in this system. The encounter kernel depends on three encounter mechanisms—Brownian motion (β_M), differential settling (i.e., sinking; β_S), and turbulent water motion (β_T)—which are additive but have different magnitudes of influence (*60*). Given that turbulence was not a factor for encounter rates derived from empirical measurements (Fig. 3I), β was expressed as

$$\beta = \beta_M + \beta_S \tag{4}$$

For modeled environmental encounter rates, which included two relevant ocean turbulence regimes (see below; fig. S13, A and B), we expressed β as the sum of all encounter kernels

$$\beta = \beta_M + \beta_S + \beta_T \tag{5}$$

Individual encounter kernels were calculated as

$$\beta_M = \frac{2kT(r_1 + r_2)^2}{3\mu\ (r_1 r_2)} \tag{6}$$

$$\beta_S = \pi\ (r_1 + r_2)^2\ |\ w_2 - w_1\ | \tag{7}$$

$$\beta_T = 1.3\left(\frac{\varepsilon}{\nu}\right)^{0.5}\ (r_1 + r_2)^3 \tag{8}$$

where k is the Boltzmann constant, T is temperature, μ is dynamic viscosity, r is the radius, w is the sinking velocity (calculated from Stokes′ Law; see below), ε is the dissipation rate of turbulent kinetic energy, and ν is the kinematic viscosity. The numbered subscripts (i.e., 1 and 2) indicate two entities encountering each other (e.g., host cells encountering viruses) (*50*, *61*). The values of the defined variables are described in table S5.

For the calculation of β_s, we calculated the sinking rates of *E. huxleyi* cells using Stokes′ law (*62*)

$$w = \frac{2r^2(\rho_E - \rho)g}{9\mu} \tag{9}$$

where r denotes the radius of either the cell (r_c) or coccolith (r_L), ρ is the density of seawater, g is the gravitational acceleration, and μ is the dynamic viscosity (table S5). For cells, sinking velocities were calculated with measured radii and densities given in table S5 to determine β_S (Eq. 7). For free coccoliths, we used a directly measured sinking rate (0.205 m day^{-1}) (*51*).

Calculations used the following environmentally observed values for entity concentrations: calcified cells, 10^3 cells ml^{-1}; naked cells, 10^2 cells ml^{-1} [10:1 calcified:naked cells (*36*); coccoliths, 5×10^4 coccoliths ml^{-1} (50:1 coccolith:calcified cell ratio); and viruses, 3×10^4 (30:1 calcified cell:virus ratio) (*20*)]. Coccoliths:calcified cells and calcified cells:virus ratios were empirically determined via environmental data from the North Atlantic Virus of Coccolithophores Expedition (NA-VICE) (*20*). Calculations were done for calm and stormy conditions ($\varepsilon = 10^{-8}$ and 10^{-3} m^2 s^{-3}, respectively); these values span the range of observed dissipation rates in ocean systems (*63*).

We determined the time to encounter between entities (fig. S13, C and D) (28) by rearranging Eq. 3 as

$$\frac{C_1}{E} = \frac{1}{\beta C_2} \tag{10}$$

Note that our estimates of encounter rates and "time to encounter" are likely under- and overestimates, respectively, given that we used conservative values for coccolith:virus and coccolith:cell ratios.

Adsorption efficiencies of coccoliths adsorbing to cells (α, cell^{-1}) were calculated using the ratio of the adsorption and encounter rates in Eqs. 2 and 3

$$\alpha = \frac{A}{E} \tag{11}$$

Efficiencies were expressed as a percentage for plotting (100*α; Fig. 3J).

To determine whether a cell's encounter rate with viroliths is higher than its rate of encounter with viruses, we calculated

$$E_{VL} = {E_L}^* X \tag{12}$$

where E_{VL} is the per-cell encounter rate of cells (calcified and naked) with viroliths (viroliths cell^{-1} day^{-1}), E_L is the per-cell encounter rate of cells with coccoliths (coccoliths cell^{-1} day^{-1}), and X is the fraction of coccoliths that are viroliths (adsorbed virus coccolith^{-1}). We wanted to know when $E_{VL} > E_V$, where E_V is the per-cell encounter rate of cells with viruses (virus cell^{-1} day^{-1})

$$E_L^* X > E_V \tag{13}$$

This equation was rearranged to

$$X > \frac{E_V}{E_L} \tag{14}$$

We substituted the encounter rates E_L and E_V, calculated as described in Eqs. 3 to 8, and normalized by cell concentration, to solve for X, the fraction of coccoliths that must be viroliths for cells receive more viruses via encounters with viroliths than with free viruses.

Viroliths

Coccoliths were isolated using methods described above. A total of 600 μl of a coccolith stock (coccoliths suspended in 0.22-μm filtered seawater; 2.91×10^9 coccoliths ml^{-1}) was added to a EhV207 lysate (0.45 μm filtered; 47 ml at 8.40×10^8 virus ml^{-1}) for a EhV:coccolith ratio of ~23:1 and incubated for ~2 hours, allowing for viral adsorption to coccoliths. The coccolith-virus suspension was then filtered

under gentle vacuum onto a 1.2-μm pore size polycarbonate filter (Isopore, EMD Millipore) and washed once with 5 ml of filtered seawater (0.22 μm) to remove free viruses. Rinsed viroliths were resuspended in 7 ml of filtered seawater and gently centrifuged (~3000*g* for 5 min at room temperature; swing bucket rotor; Fisher Scientific Centrific Model 225 centrifuge). Six milliliters of supernatant was removed, leaving 1 ml for final virolith suspension. Viroliths were used in a similar experimental setup to that described for exogenous coccoliths additions, except with coccolith:cell ratio of 50:1 (Fig. 4, B to D). Virolith adsorption and virus concentrations were determined using flow cytometry.

To quantify the degree of virus attachment to coccoliths for this procedure, the total number of viruses was measured at each step of virolith generation process. Free viruses (EhV207) were exposed to coccoliths for ~2 hours at an average ratio of ~31 EhVs per coccolith and subsequently filtered as above. After on-filter rinsing, centrifugation, and resuspension of viroliths (0.5 ml), 3% of the EhVs from the starting lysate (gray) were found associated with rinsed viroliths (fig. S14A, black arrow). The total number of viruses in the subsequent virolith resuspension (fig. S14A, black, open circles) was compared to that in the supernatant after removal of those viroliths via centrifugation (black, closed circles). The difference in virus concentration between these samples represented the number of adsorbed viruses. An average of 0.76 ± 0.15 EhVs was measured per coccolith using this procedure. The strength of EhV attachment onto viroliths was further tested by additional pelleting via gentle centrifugation and resuspension in fresh filtered seawater (0.5 ml; light blue) and compared to the supernatant alone (forest green). This analysis revealed 1.02 ± 0.03 EhVs per coccolith.

Most probable number assays

The most probable number (MPN) method was used to measure the impact of coccoliths on the number of infectious viruses. Two 96-well plates were loaded with 200 μl of 1×10^6 naked CCMP374 cells and one plate received a coccolith:cell ratio of 50:1. The outer wells of each plate were left blank to remove possible impacts of evaporation. The first column of each plate was an uninfected control ($n = 6$, technical replicates). The subsequent nine columns were loaded with 20 μl of serially diluted viruses; dilution factors (moving from left to right) ranged from 5 to 1.95×10^6. Both plates were sealed with parafilm to prevent evaporation and incubated at 18°C under a 14:10 L:D cycle at 150 μmol photons m^{-2} s^{-1}. After 2 weeks, the optical density (OD) at 750 nm of cells was measured using a SpectraMax Gemini XS plate reader. The number of wells cleared in each plate was determined both visually and quantitatively (ΔOD_{750} of ~0; the value of a lysed culture). The number of infectious viruses with and without coccoliths was calculated using the U.S. Environmental Protection Agency MPN calculator (https://mostprobablenumbercalculator.epa.gov/mpnForm) set to a fivefold serial dilution with Cornish and Fisher limits as the approximation type. Images for each plate have been incorporated into Fig. 5 (A and B).

Time series experiments

Two different experimental setups were used to assess the impact of free coccoliths on infection dynamics and to test the ability of viroliths to increase virus-host encounter rates. First, a small volume (200-μl) experiment using a 96-well microtiter plate was set up as per the MPN assay above and the change in OD_{750} was measured for infected cells with and without coccoliths at virus:host ratios corresponding to: 10:1, 1:1, 0.1:1, and 0.01:1. The 96-well plate was loaded with naked CCMPP374 cells at a starting concentration of 1×10^5 cells ml^{-1}. One half of the plate represented cells only; the other half received free coccoliths at a 50:1 coccolith to cell ratio. The first column in each treatment set was an uninfected control and subsequent columns were infected with EhVs at different virus:host ratios (as above). Treatments were set up in 3 ml of total volumes after which 200 μl was aliquoted into each well for technical replicates ($n = 8$). OD_{750} values were measured daily over a 240-hour postinfection time course. Data have been incorporated into Fig. 5 (C to E).

We also performed larger volume (40 ml) experiments in biological triplicates to directly test the relative ability of viroliths to facilitate and accelerate infection. Naked cells were exposed to either thoroughly washed viroliths and the accompanying virolith supernatant and monitoring host and virus concentrations, along with the degree of virolith attachment to cells (fig. S14, B to D). The volume of virolith resuspension and virolith supernatant added to a naked cell culture (average of ~4.43×10^4 cells ml^{-1}, starting concentration) was used to produce a 50:1 coccolith:cell ratio (as per previous experiments; Fig. 4, B to D).

The relative infection dynamics of viroliths and virus-only treatments were tested at a range of virus:host ratios (0.01 to 5; fig. S16). Virolith additions were performed across a range of coccolith:cell ratios (0.1:1 to 50:1) using two independent coccolith isolation methods [FACS (fig. S16A) and the density centrifugation used throughout this manuscript (see Methods above; fig. S16B)]. Free viruses (EhV207) were exposed to coccoliths for 2 hours before addition. We note that both the virolith and free virus treatments contained the same starting virus:host ratio. The results from these experiments are shown in Fig. 5F and fig. S16 (A and B).

Data and statistical analysis

All data and statistical analysis were performed using R (version 3.6) with the packages "ggplot2" (*64*) for plotting; "mgcv" (*65*–*67*), "mgcViz" (*68*), and "tidymv" (*69*) for GAMM, data visualization, and plotting; "phytools" (*70*) for analysis of photophysiological data; and "FSA" (*71*) for post hoc analysis of Kruskal-Wallis rank sum test. See table S1 for the statistical summary.

For GAMM, the percentage of calcified cells (Fig. 2, A and C, and fig. S3), as well as cell and virus concentrations (fig. S14, C to F) were fitted to a smoothed factor interaction of time (hour) and treatment penalized with cubic regression splines and unique replicate identifier (ID) (i.e., replicate ID based on each experiment) as the random factor. An autoregressive (AR-1) correlation structure was added between treatment and unique replicate IDs to account for successive measurements over time. Additive models connect individual data points by smoothing and setting the population mean of each dataset to zero. The optimum model was selected using the Akaike information criterion. Computed *P* values indicate the significance of the smoothing terms. Pairwise comparisons between treatments were performed by obtaining the difference of the smoothed GAMM models and plotting them with their associated 95% confidence intervals (fig. S15, A and B) (*72*). The treatments in the rows were subtracted from the treatments in the columns. A nonzero difference between the two smooth was inferred as a significant difference.

Supplementary Materials

This PDF file includes:
Figs. S1 to S16
Tables S1 to S5
References

Other Supplementary Material for this manuscript includes the following:
Movie S1

View/request a protocol for this paper from *Bio-protocol*.

REFERENCES AND NOTES

1. A. R. Taylor, M. A. Russell, G. M. Harper, T. F. T. Collins, C. Brownlee, Dynamics of formation and secretion of heterococcoliths by *Coccolithus pelagicus* ssp *braarudii*. *Eur. J. Phycol.* **42**, 125–136 (2007).
2. L. Mackinder, G. Wheeler, D. Schroeder, U. Riebesell, C. Brownlee, Molecular mechanisms underlying calcification in coccolithophores. *Geomicrobiol. J.* **27**, 585–595 (2010).
3. P. L. A. M. Corstjens, A. Van Der Kooij, C. Linschooten, G.-J. Brouwers, P. Westbroek, E. W. De Vrind-De Jong, Gpa, a calcium-binding protein in the coccolithophorid *Emiliania huxleyi* (Prymnesiophyceae). *J. Phycol.* **34**, 622–630 (1998).
4. C. E. Walker, A. R. Taylor, G. Langer, G. M. Durak, S. Heath, I. Probert, T. Tyrrell, C. Brownlee, G. L. Wheeler, The requirement for calcification differs between ecologically important coccolithophore species. *New Phytol.* **220**, 147–162 (2018).
5. C. T. Johns, A. Grubb, J. I. Nissimov, F. Natale, V. Knapp, A. Mui, H. Fredricks, B. A. S. Van Mooy, K. D. Bidle, The mutual interplay between calcification and coccolithovirus infection. *Environ. Microbiol.* **21**, 1896–1915 (2019).
6. J. Young, S. Davis, P. Bown, S. Mann, Coccolith ultrastructure and biomineralisation. *J. Struct. Biol.* **126**, 195–215 (1999).
7. J. R. Young, P. R. Brown, J. A. Lees, Nannotax3 website. *International Nannoplankton Association* (2017);www.mikrotax.org/Nannotax3.
8. K. Hagino, E. M. Bendif, J. R. Young, K. Kogame, I. Probert, Y. Takano, T. Horiguchi, C. de Vargas, H. Okada, New evidence for morphological and genetic variation in the cosmopolitan coccolithophore *Emiliania huxleyi* (Prymnesiophyceae) from the cox1b-atp4 genes. *J. Phycol.* **47**, 1164–1176 (2011).
9. S. Blanco-Ameijeiras, M. Lebrato, H. M. Stoll, D. Iglesias-Rodriguez, M. N. Müller, A. Méndez-Vicente, A. Oschlies, Phenotypic variability in the coccolithophore *Emiliania huxleyi*. *PLOS ONE* **11**, e0157697 (2016).
10. E. Paasche, A review of the coccolithophorid *Emiliania huxleyi* (Prymnesiophyceae), with particular reference to growth, coccolith formation, and calcification-photosynthesis interactions. *Phycologia* **40**, 503–529 (2001).
11. P. Von Dassow, G. Van Den Engh, D. Iglesias-Rodriguez, J. R. Gittins, Calcification state of coccolithophores can be assessed by light scatter depolarization measurements with flow cytometry. *J. Plankton Res.* **34**, 1011–1027 (2012).
12. W. M. Balch, K. Kilpatrick, P. M. Holligan, T. Cucci, Coccolith production and detachment by *Emiliania huxleyi* (Prymnesiophyceae). *J. Phycol.* **29**, 566–575 (1993).
13. W. M. Balch, P. M. Holligan, S. G. Ackleson, K. J. Voss, Biological and optical properties of mesoscale coccolithophore blooms in the Gulf of Maine. *Limnol. Oceanogr.* **36**, 629–643 (1991).
14. H. R. Gordon, T. J. Smyth, W. M. Balch, G. Chris Boynton, G. A. Tarran, Light scattering by coccoliths detached from *Emiliania huxleyi*. *Appl. Optics* **48**, 6059–6073 (2009).
15. P. G. Matson, T. M. Ladd, E. R. Halewood, R. P. Sangodkar, B. F. Chmelka, M. D. Iglesias-Rodriguez, Intraspecific differences in biogeochemical responses to thermal change in the coccolithophore *Emiliania huxleyi*. *PLOS ONE.* **11**, e0162313 (2016).
16. J. B. E. Ramos, K. G. Schulz, S. Febiri, U. Riebesell, Photoacclimation to abrupt changes in light intensity by *Phaeodactylum tricornutum* and *Emiliania huxleyi*: The role of calcification. *Mar. Ecol. Prog. Ser.* **452**, 11–26 (2012).
17. I. Zondervan, The effects of light, macronutrients, trace metals and CO2 on the production of calcium carbonate and organic carbon in coccolithophores—A review. *Deep. Res. Part II Top. Stud. Oceanogr.* **54**, 521–537 (2007).
18. B. D'Amario, P. Ziveri, M. Grelaud, A. Oviedo, *Emiliania huxleyi* coccolith calcite mass modulation by morphological changes and ecology in the Mediterranean Sea. *PLOS ONE* **13**, e0201161 (2018).
19. M. L. Pedrotti, S. Fiorini, M. E. Kerros, J. J. Middelburg, J. P. Gattuso, Variable production of transparent exopolymeric particles by haploid and diploid life stages of coccolithophores grown under different CO_2 concentrations. *J. Plankton Res.* **34**, 388–398 (2012).
20. C. P. Laber, J. E. Hunter, F. Carvalho, J. R. Collins, E. J. Hunter, B. M. Schieler, E. Boss, K. More, M. Frada, K. Thamatrakoln, C. M. Brown, L. Haramaty, J. Ossolinski, H. Fredricks, J. I. Nissimov, R. Vandzura, U. Sheyn, Y. Lehahn, R. J. Chant, A. M. Martins, M. J. L. Coolen, A. Vardi, G. R. Ditullio, B. A. S. Van Mooy, K. D. Bidle, Coccolithovirus facilitation of carbon export in the North Atlantic. *Nat. Microbiol.* **3**, 537–547 (2018).
21. A. Winter, Z. Reiss, B. Luz, Distribution of living coccolithophore assemblages in the Gulf of Elat ('Aqaba). *Mar. Micropaleontol.* **4**, 197–223 (1979).
22. J. Young, M. Geisen, Xenospheres–Associations of coccoliths resembling coccospheres. *J. Nannoplankton Res.* **24**, 27–35 (2002).
23. S. M. Patil, R. Mohan, S. A. Jafar, S. Gazi, Xenospheres and anomalous coccospheres from plankton samples of the southern Indian Ocean. *J. Nannoplankton Res.* **36**, 133–136 (2016).
24. L. C. M. Mackinder, C. A. Worthy, G. Biggi, M. Hall, K. P. Ryan, A. Varsani, G. M. Harper, W. H. Wilson, C. Brownlee, D. C. Schroeder, A unicellular algal virus, *Emiliania huxleyi* virus 86, exploits an animal-like infection strategy. *J. Gen. Virol.* **90**, 2306–2316 (2009).
25. G. Bratbak, J. K. Egge, M. Heldal, Viral mortality of the marine alga *Emiliania huxleyi* (Haptophyceae) and termination of algal blooms. *Mar. Ecol. Prog. Ser.* **93**, 39–48 (1993).
26. S. Jacquet, M. Heldal, D. Iglesias-Rodriguez, A. Larsen, W. Wilson, G. Bratbak, Flow cytometric analysis of an *Emiliana huxleyi* bloom terminated by viral infection. *Aquat. Microb. Ecol.* **27**, 111–124 (2002).
27. A. Vardi, L. Haramaty, B. A. S. Van Mooy, H. F. Fredricks, S. A. Kimmance, A. Larsen, K. D. Bidle, Host-virus dynamics and subcellular controls of cell fate in a natural coccolithophore population. *Proc. Natl. Acad. Sci. U.S.A.* **109**, 19327–19332 (2012).
28. B. Knowles, J. A. Bonachela, M. J. Behrenfeld, K. G. Bondoc, B. B. Cael, C. A. Carlson, N. Cieslik, B. Diaz, H. L. Fuchs, J. R. Graff, J. A. Grasis, K. H. Halsey, L. Haramaty, C. T. Johns, F. Natale, J. I. Nissimov, B. M. Schieler, K. Thamatrakoln, T. F. Thingstad, S. Våge, C. Watkins, T. K. Westberry, K. D. Bidle, Temperate infection in a virus-host system previously known for virulent dynamics. *Nat. Commun.* **11**, 4626 (2020).
29. H. E. K. Smith, T. Tyrrell, A. Charalampopoulou, C. Dumousseaud, O. J. Legge, S. Birchenough, L. R. Pettit, R. Garley, S. E. Hartman, M. C. Hartman, N. Sagoo, C. J. Daniels, E. P. Achterberg, D. J. Hydes, Predominance of heavily calcified coccolithophores at low $CaCO_3$ saturation during winter in the Bay of Biscay. *Proc. Natl. Acad. Sci. U.S.A.* **109**, 8845–8849 (2012).
30. M. D. Dimiza, M. V. Triantaphyllou, E. Malinverno, S. Psarra, P. Mara, A. Lagaria, A. Birli, P. Syriopoulou, A. Zapantis, The composition and distribution of living coccolithophores in the northeastern Mediterranean Sea. "Coccolithophores 2014" INA Workshop on extant coccolithophore research. *J. Nannoplankton Res.* **34**, 80 (2014).
31. J. Bollmann, U. Wortmann, The Electronic Microfossil Image Data Base System (EMIDAS) (2020).
32. J. R. Young, P. Westbroek, Genotypic variation in the coccolithophorid species *Emiliania huxleyi*. *Mar. Micropaleontol.* **18**, 5–23 (1991).
33. P. G. Matson, L. Washburn, E. A. Fields, C. Gotschalk, T. M. Ladd, D. A. Siegel, Z. S. Welch, M. D. Iglesias-Rodriguez, Formation, development, and propagation of a rare coastal coccolithophore bloom. *J. Geophys. Res. Ocean.* **124**, 3298–3316 (2019).
34. T. Tyrrell, A. Merico, in *Coccolithophores* (Springer Berlin Heidelberg, Berlin, Heidelberg, 2004);http://link.springer.com/10.1007/978-3-662-06278-4_4, pp. 75–97.
35. L. Cros, A. Kleijne, A. Zeltner, C. Billard, J. R. Young, New examples of holococcolith-heterococcolith combination coccospheres and their implications for coccolithophorid biology. *Mar. Micropaleontol.* **39**, 1–34 (2000).
36. M. J. Frada, K. D. Bidle, I. Probert, C. de Vargas, In situ survey of life cycle phases of the coccolithophore *Emiliania huxleyi* (Haptophyta). *Environ. Microbiol.* **14**, 1558–1569 (2012).
37. A. Gal, R. Wirth, J. Kopka, P. Fratzl, D. Faivre, A. Scheffel, Macromolecular recognition directs calcium ions to coccolith mineralization sites. *Science* **353**, 590–593 (2016).
38. E. Fox, E. Meyer, N. Panasiak, A. R. Taylor, Calcein staining as a tool to investigate coccolithophore calcification. *Front. Mar. Sci.* **5**, 326 (2018).
39. B. M. Schieler, M. V. Soni, C. M. Brown, M. J. L. Coolen, H. Fredricks, B. A. S. Van Mooy, D. J. Hirsh, K. D. Bidle, Nitric oxide production and antioxidant function during viral infection of the coccolithophore *Emiliania huxleyi*. *ISME J.* **13**, 1019–1031 (2019).
40. X. Mari, F. Rassoulzadegan, C. P. D. Brussaard, P. Wassmann, Dynamics of transparent exopolymeric particles (TEP) production by *Phaeocystis globosa* under N- or P-limitation: A controlling factor of the retention/export balance. *Harmful Algae* **4**, 895–914 (2005).
41. J. Xu, L. T. Bach, K. G. Schulz, W. Zhao, K. Gao, U. Riebesell, The role of coccoliths in protecting *Emiliania huxleyi* against stressful light and UV radiation. *Biogeosciences* **13**, 4637–4643 (2016).
42. F. M. Monteiro, L. T. Bach, C. Brownlee, P. Bown, R. E. M. Rickaby, A. J. Poulton, T. Tyrrell, L. Beaufort, S. Dutkiewicz, S. Gibbs, M. A. Gutowska, R. Lee, U. Riebesell, J. Young, A. Ridgwell, Why marine phytoplankton calcify. *Sci. Adv.* **2**, e1501822 (2016).
43. P. van der Wal, E. W. de Jong, P. Westbroek, W. C. de Bruijn, A. A. Mulder-Stapel, Ultrastructural polysaccharide localization in calcifying and naked cells of the coccolithophorid *Emiliania huxleyi*. *Protoplasma* **118**, 157–168 (1983).

44. C. Brownlee, G. L. Wheeler, A. R. Taylor, Coccolithophore biomineralization: New questions, new answers. *Semin. Cell Dev. Biol.* **46**, 11–16 (2015).
45. D. Klaveness, *Emiliania huxleyi* (Lohmann) Hay & Mohler. III. Mineral deposition and the origin of the matrix during coccolith formation. *Protist* **12**, 217–224 (1976).
46. C. E. Walker, S. E. Heath, D. L. Salmon, N. Smirnoff, G. Langer, A. R. Taylor, C. Brownlee, G. L. Wheeler, An extracellular polysaccharide-rich organic layer contributes to organization of the coccosphere in coccolithophores. *Front. Mar. Sci.* **5**, 306 (2018).
47. M. N. Müller, B. Kisakürek, D. Buhl, R. Gutperlet, A. Kolevica, U. Riebesell, H. Stoll, A. Eisenhauer, Response of the coccolithophores *Emiliania huxleyi* and Coccolithus braarudii to changing seawater Mg^{2+} and Ca^{2+} concentrations: Mg/Ca, Sr/Ca ratios and $\delta^{44/40}Ca$, $\delta^{26/24}Mg$ of coccolith calcite. *Geochim. Cosmochim. Acta* **75**, 2088–2102 (2011).
48. A. J. Poulton, J. R. Young, N. R. Bates, W. M. Balch, Biometry of detached *Emiliania huxleyi* coccoliths along the Patagonian Shelf. *Mar. Ecol. Prog. Ser.* **443**, 1–17 (2011).
49. I. N. McCave, Size spectra and aggregation of suspended particles in the deep ocean. *Deep Sea Res. Part I Oceanogr. Res. Pap.* **31**, 329–352 (1984).
50. T. Kiørboe, E. Saiz, Planktivorous feeding in calm and turbulent environments, with emphasis on copepods. *Mar. Ecol. Prog. Ser.* **122**, 135–145 (1995).
51. H. Zhang, H. Stoll, C. Bolton, X. Jin, C. Liu, Technical note: A refinement of coccolith separation methods: Measuring the sinking characteristics of coccoliths. *Biogeosciences.* **15**, 4759–4775 (2018).
52. J. R. Collins, B. R. Edwards, K. Thamatrakoln, J. E. Ossolinski, G. R. DiTullio, K. D. Bidle, S. C. Doney, B. A. S. Van Mooy, The multiple fates of sinking particles in the North Atlantic Ocean. *Global Biogeochem. Cycles* **29**, 1471–1494 (2015).
53. H. Takano, E. Manabe, M. Hirano, M. Okazaki, J. G. Burgess, N. Nakamura, T. Matsunaga, Development of a rapid isolation procedure for coccolith ultrafine particles produced by coccolithophorid algae. *Appl. Biochem. Biotechnol.* **39**, 239–247 (1993).
54. Homer, *The Odyssey* (W. Heinemann; G.P. Putnam's sons, London; New York, 1919).
55. R. R. L. Guillard, in *Culture of Marine Invertebrate Animals*, W. L. Smith, M. H. Chanley, Eds. (Plenum Press, USA, 1975), pp. 29–60.
56. T. M. Ladd, J. A. Bullington, P. G. Matson, R. M. Kudela, M. Débora Iglesias-Rodríguez, Exposure to oil from the 2015 Refugio spill alters the physiology of a common harmful algal bloom species, *Pseudo-nitzschia australis*, and the ubiquitous coccolithophore, *Emiliania huxleyi*. *Mar. Ecol. Prog. Ser.* **603**, 61–78 (2018).
57. S. Blanco-Ameijeiras, M. Lebrato, H. M. Stoll, M. D. Iglesias-Rodriguez, A. Méndez-Vicente, S. Sett, M. N. Müller, A. Oschlies, K. G. Schulz, Removal of organic magnesium in coccolithophore calcite. *Geochim. Cosmochim. Acta* **89**, 226–239 (2012).
58. M. Y. Gorbunov, P. G. Falkowski, in *Photosynthesis: Fundamental Aspects to Global Perspectives*, D. Bruce, A. van der Est, Eds. (Allen Press, 2004), pp. 1029–1031.
59. C. P. D. Brussaard, Optimization of procedures for counting viruses by flow cytometry. *Appl. Environ. Microbiol.* **70**, 1506–1513 (2004).
60. T. Kiørboe, A mechanistic approach to plankton ecology. *ALSO Web Lect.* **1**, 1–91 (2009).
61. A. B. Burd, G. A. Jackson, Particle aggregation. *Annu. Rev. Mar. Sci.* **1**, 65–90 (2009).
62. S. Vogel, *Life in Moving Fluids: The Physical Biology of Flow-Revised and Expanded* (Princeton Univ. Press, ed. 2, 2020).
63. H. L. Fuchs, G. P. Gerbi, Seascape-level variation in turbulence- and wave-generated hydrodynamic signals experienced by plankton. *Prog. Oceanogr.* **141**, 109–129 (2016).
64. H. Wickham, *ggplot2: Elegant Graphics for Data Analysis* (Springer-Verlag, 2016);https://ggplot2.tidyverse.org.
65. S. N. Wood, Stable and efficient multiple smoothing parameter estimation for generalized additive models. *J. Am. Stat. Assoc.* **99**, 673–686 (2004).
66. S. N. Wood, Fast stable restricted maximum likelihood and marginal likelihood estimation of semiparametric generalized linear models. *J. R. Stat. Soc.* **73**, 3–36 (2011).
67. S. N. Wood, in *Generalized Additive Models: An Introduction with R* (Chapman and Hall/CRC, ed. 2, 2017).
68. M. Fasiolo, R. Nedellec, Y. Goude, S. N. Wood, Scalable visualisation methods for modern generalized additive models. *J. Comput. Graph. Stat.* 29, 78-86 (2020)..
69. S. Coretta, J. van Rij, M. Wieling, tidymv: Tidy model visualisation for generalised additive models. R package version 3.0.0. (2021);https://github.com/stefanocoretta/tidymv.
70. L. J. Revell, phytools: An R package for phylogenetic comparative biology (and other things). *Methods Ecol. Evol.* **3**, 217–223 (2012).
71. D. H. Ogle, J. C. Doll, P. Wheeler, A. Dinno, FSA: Fisheries stock analysis. R package version 0.9.3. (2021);https://github.com/droglenc/FSA.
72. N. L. Rose, H. Yang, S. D. Turner, G. L. Simpson, An assessment of the mechanisms for the transfer of lead and mercury from atmospherically contaminated organic soils to lake sediments with particular reference to Scotland, UK. *Geochim. Cosmochim. Acta* **82**, 113–135 (2012).
73. I. Jakob, M. A. Chairopoulou, M. Vučak, C. Posten, U. Teipel, Biogenic calcite particles from microalgae—Coccoliths as a potential raw material. *Eng. Life Sci.* **17**, 605–612 (2017).
74. T. Castberg, R. Thyrhaug, A. Larsen, R. A. Sandaa, M. Heldal, J. L. Van Etten, G. Bratbak, Isolation and characterization of a virus that infects *Emiliania huxleyi* (Haptophyta). *J. Phycol.* **38**, 767–774 (2002).

Acknowledgments: From UCSB, we acknowledge T. Ladd for isolating and morphotyping the *E. huxleyi* strains provided and S. Kim for assisting with shipping. From Rutgers, we acknowledge K. Thamatrakoln, B. Knowles, C. Kranzler, L. Haramaty, A. Grubb, B. Diaz, and C. Watkins for the comments and feedback during the development of this project; F. Natale and the Microbial Flow Sort Lab for assistance with cell sorting and flow cytometry optimization; and M. Pierce at the Rutgers School of Environmental and Biological Sciences (SEBS) Bio-Imaging Core Facility for the expertise in confocal microscopy. In addition, we thank and acknowledge all the scientists who provided SEM images, including K. Hagino, B. D'Amario, M. Dimiza, and O. Archontikis. Last, we also thank O. Eliason (Weizmann Institute of Science) for discussion and encouragement about coccolith isolation at the 2018 Gordon Research Conference on Marine Microbes in Lucca, Italy. **Funding:** This work was funded by grants from the Gordon and Betty Moore Foundation (award numbers 3789 and 3301 to K.D.B.) and the National Science Foundation (OCE-1537951, OCE-1459200, OCE-1559179, and OIA-2021032 to K.D.B. and OCE-1638838 to A.R.T.). The Analytical Instrumentation Facility (AIF) at North Carolina State University was supported by the State of North Carolina and the National Science Foundation (award number ECCS-1542015). P.G.M. was supported by the NASA Biodiversity and Ecological Forecasting program (grant NNX14AR62A), the Bureau of Ocean and Energy Management Ecosystem Studies program (BOEM award MC15AC00006), and NOAA in support of the Southern California Bight Marine Biodiversity Observation Network (SBC MBON). The SEBS Bio-Imaging Core is supported by NIH Shared Instrumentation Grant 1S10RR025424. **Author contributions:** C.T.J., A.R.T., M.D.I.-R., H.L.F., and K.D.B. conceptualized the project. C.T.J., A.M., K.G.B.-N., and A.R.T. collected and analyzed the data. C.T.J., K.G.B.-N., H.L.F., and K.D.B. visualized the data, arranged the figures, and wrote the manuscript. K.G.B.-N. assisted with the statistical analysis and GAMM. K.G.B.-N. and H.L.F. developed the theoretical model of environmental encounter rates and assisted with calculations for coccolith removal/encounter rates, adsorption efficiencies, and minimum virolith fractions. P.G.M., M.D.I.-R., and A.R.T. provided the SEM images and *E. huxleyi* morphotypes used in this study. A.R.T., P.G.M, M.D.I.-R., H.L.F., and K.D.B. provided funding sources for the project. All authors helped review and edit the manuscript. **Competing interests:** The authors declare that they have no competing interests. **Data and materials availability:** All data needed to evaluate the conclusions in the paper are present in the paper and/or the Supplementary Materials. All data, materials, and code have been submitted to BCO-DMO, Dataverse, and GitHub under the following project sites [BCO-DMO (www.bco-dmo.org/project/820228 and www.bco-dmo.org/project/681437), Dataverse (https://doi.org/10.7910/DVN/TLKUI0), and GitHub (https://github.com/cjohns89/Coccolith-adsorption)].

Submitted 10 May 2022
Accepted 16 December 2022
Published 20 January 2023
10.1126/sciadv.adc8728